

# A Simple Numerical Model of Calcium Spark Formation and Detection in Cardiac Myocytes

Gregory D. Smith,\* Joel E. Keizer,# Michael D. Stern,\$ W. Jonathan Lederer,† and Heping Cheng§

\*Mathematical Research Branch, National Institutes of Health, Bethesda, Maryland 20814; #Institute for Theoretical Dynamics and Section on Neurobiology, Physiology, and Behavior, University of California, Davis, California 95616; §Laboratory of Cardiovascular Science, Gerontology Research Center, National Institutes of Health, Baltimore, Maryland 21224; and †Department of Molecular Biology and Biophysics, University of Maryland, Baltimore, Maryland 21201 USA

**ABSTRACT** The elementary events of excitation-contraction coupling in heart muscle are  $\text{Ca}^{2+}$  sparks, which arise from one or more ryanodine receptors in the sarcoplasmic reticulum (SR). Here a simple numerical model is constructed to explore  $\text{Ca}^{2+}$  spark formation, detection, and interpretation in cardiac myocytes. This model includes  $\text{Ca}^{2+}$  release, cytosolic diffusion, resequestration by SR  $\text{Ca}^{2+}$ -ATPases, and the association and dissociation of  $\text{Ca}^{2+}$  with endogenous  $\text{Ca}^{2+}$ -binding sites and a diffusible indicator dye (fluo-3). Simulations in a homogeneous, isotropic cytosol reproduce the brightness and the time course of a typical cardiac  $\text{Ca}^{2+}$  spark, but underestimate its spatial size ( $\sim 1.1 \mu\text{m}$  vs.  $\sim 2.0 \mu\text{m}$ ). Back-calculating  $[\text{Ca}^{2+}]_i$  by assuming equilibrium with indicator fails to provide a good estimate of the free  $\text{Ca}^{2+}$  concentration even when using blur-free fluorescence data. A parameter sensitivity study reveals that the mobility, kinetics, and concentration of the indicator are essential determinants of the shape of  $\text{Ca}^{2+}$  sparks, whereas the stationary buffers and pumps are less influential. Using a geometrically more complex version of the model, we show that the asymmetric shape of  $\text{Ca}^{2+}$  sparks is better explained by anisotropic diffusion of  $\text{Ca}^{2+}$  ions and indicator dye rather than by subsarcomeric inhomogeneities of the  $\text{Ca}^{2+}$  buffer and transport system. In addition, we examine the contribution of off-center confocal sampling to the variance of spark statistics.

## INTRODUCTION

The recent discovery of “ $\text{Ca}^{2+}$  sparks” in cardiac myocytes via confocal microfluorimetry (Cheng et al., 1993) has greatly advanced our understanding of the subcellular events responsible for  $\text{Ca}^{2+}$  release from the sarcoplasmic reticulum (SR). The  $\text{Ca}^{2+}$  spark has been identified as an “elementary”  $\text{Ca}^{2+}$  release event under physiological conditions and may arise from the opening of a single SR  $\text{Ca}^{2+}$  release channel/ryanodine receptor (RyR) or a small number of such channels acting in concert (Cheng et al., 1993; Cannell et al., 1995; López-López et al., 1995; see also Lipp and Niggli, 1996; for a review see Cheng et al., 1996b). During cardiac excitation-contraction coupling, the stochastic recruitment of  $\text{Ca}^{2+}$  sparks by L-type  $\text{Ca}^{2+}$  channels in the sarcolemmal (SL) membrane is controlled by the mechanism of  $\text{Ca}^{2+}$ -induced  $\text{Ca}^{2+}$  release (CICR) (Fabiato, 1985). Summation of  $\text{Ca}^{2+}$  sparks gives rise to the global  $[\text{Ca}^{2+}]_i$  transient, which activates the contractile myofilaments. Although there are important differences, localized intracellular  $\text{Ca}^{2+}$  release events similar to cardiac  $\text{Ca}^{2+}$  sparks have been observed in skeletal (Tsugorka et al., 1995; Klein et al., 1996) and smooth muscle (Nelson et al., 1995) that express different isoforms of the ryanodine receptor and have different ultrastructural organization of the cells. Furthermore, local  $\text{Ca}^{2+}$  elevations, dubbed “ $\text{Ca}^{2+}$

puffs” and “ $\text{Ca}^{2+}$  blips,” have been observed in *Xenopus* oocytes (Yao et al., 1995; Parker and Yao, 1996) containing the inositol trisphosphate receptor, the second major branch of the intracellular  $\text{Ca}^{2+}$  release channel superfamily (Berridge, 1993).

Theoretically, the formation of a  $\text{Ca}^{2+}$  spark can be viewed as a reaction-diffusion problem involving  $\text{Ca}^{2+}$  release from the SR, cytosolic  $\text{Ca}^{2+}$  diffusion, reaction of  $\text{Ca}^{2+}$  with various  $\text{Ca}^{2+}$ -binding proteins (endogenous  $\text{Ca}^{2+}$  “buffers”), and re-sequestration of  $\text{Ca}^{2+}$  into the SR via ATP-dependent transport. The  $\text{Ca}^{2+}$ -indicator dye itself is a molecular species capable of binding  $\text{Ca}^{2+}$  and affecting its transport. The effect of both exogenous and endogenous  $\text{Ca}^{2+}$  buffers is complicated by the fact that these species may be mobile and thus capable of diffusing in both free and bound forms (Harkins et al., 1993; Roberts, 1993; Wagner and Keizer, 1994). Analysis of  $\text{Ca}^{2+}$  sparks further requires a theoretical framework by which one can infer the physiologically relevant free  $\text{Ca}^{2+}$  elevation from the experimentally measured signal, the indicator fluorescence. Initial observations and calculations suggested that the SR  $\text{Ca}^{2+}$  efflux during a  $\text{Ca}^{2+}$  spark is of the order of 3 pA (Cheng et al., 1993; Blatter et al., 1997), that the decay rate is dominated by diffusion (Cheng et al., 1995; Gómez et al., 1996), and that the rate of  $\text{Ca}^{2+}$  transport into the SR can influence the time-course of the  $\text{Ca}^{2+}$  spark (Gómez et al., 1996). However, because of the many fluxes involved in  $\text{Ca}^{2+}$  spark formation and other experimental and theoretical issues related to their detection (see Methods), quantitative modeling is warranted for understanding various mechanisms of  $\text{Ca}^{2+}$  spark formation and needed to correctly interpret data from fluorescence measurement.

Received for publication 2 October 1997 and in final form 8 April 1998.

Address reprint requests to Dr. Heping Cheng, Laboratory of Cardiovascular Science, Gerontology Research Center, NIA, NIH, 5600 Nathan Shock Drive, Baltimore, MD 21224. Tel.: (410) 558-8634; Fax: (410) 558-8150; E-mail: chengp@grc.nia.nih.gov.

© 1998 by the Biophysical Society

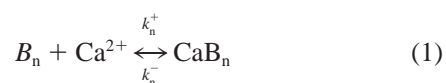
0006-3495/98/07/15/18 \$2.00

Many authors have contributed to the theoretical framework within which these calculations of  $\text{Ca}^{2+}$  sparks are performed (Neher, 1986; Stern, 1992a; Allbritton et al., 1992; Wagner and Keizer, 1994; Cannell et al., 1995). Preliminary calculations of  $\text{Ca}^{2+}$  puffs similar to those presented here were performed in an analysis of the validity of the rapid buffering approximation near a  $\text{Ca}^{2+}$  source (Smith et al., 1996). These calculations included a crude coarse-graining or averaging meant to simulate the optical blurring inherent in confocal microscopic measurements, but used parameters that were more relevant to *Xenopus* oocytes than cardiac myocytes. Analytical work based on the rapid buffering approximation provides an upper bound on the source strength required to produce a given elevated  $\text{Ca}^{2+}$ -bound indicator dye profile (Smith, 1996). Most recently, Pratusевич and Balke (1996) presented simulations of  $\text{Ca}^{2+}$  sparks to explore the effect of photon noise and out-of-focus events on the fidelity of the  $\text{Ca}^{2+}$  spark measurements. Several other studies have focused on  $\text{Ca}^{2+}$  binding to membrane phospholipids as well as electrodiffusion of  $\text{Ca}^{2+}$  within the diadic space that couples RyR's to the L-type channels (Langer and Peskoff, 1996; Soeller and Cannell, 1997).

Here we extend our preliminary work on the modeling of  $\text{Ca}^{2+}$  transport during localized  $\text{Ca}^{2+}$  elevations (Cheng et al., 1993; 1995; Gómez et al., 1996; Smith, 1996; Smith et al., 1996) and present a simple numerical model of spark formation and detection. Specifically, our goal is to understand what cellular features determine the size, amplitude, and kinetics of a  $\text{Ca}^{2+}$  spark and how the spatiotemporal properties of the fluorescence signals observed in confocal imaging are related to the space-time dynamics of the underlying  $[\text{Ca}^{2+}]_i$  signal. To make the models more useful, we investigate the limits of the experimental work by exploring how the measurement of  $\text{Ca}^{2+}$  sparks perturbs the underlying free  $\text{Ca}^{2+}$  elevation. The inclusion of a realistic "point spread function" (PSF) into our calculations allows us to simulate the contribution of out-of-focus signal and to illustrate the effect of axial and radial off-center sampling of  $\text{Ca}^{2+}$  sparks. In addition, we present and discuss versions of the model that include anisotropy, subcellular inhomogeneities of  $\text{Ca}^{2+}$  handling mechanisms, and  $\text{Ca}^{2+}$  release from a spatially extended  $\text{Ca}^{2+}$  release site.

### Description of model components and fluxes

The calculations of  $\text{Ca}^{2+}$  sparks presented here assume buffering reactions of the following form:



where  $n$  is an index over each buffer species;  $B_n$  represents a buffer binding site; and  $\text{CaB}_n$  represents  $\text{Ca}^{2+}$  bound to such a site. We assume a similar form for the reaction of cytosolic  $\text{Ca}^{2+}$  with the indicator dye fluo-3, which can exist in both  $\text{Ca}^{2+}$ -free (F) and  $\text{Ca}^{2+}$ -bound (CaF) forms.

To incorporate the diffusion of  $\text{Ca}^{2+}$  and indicator dye in both forms, as well as immobilize  $\text{Ca}^{2+}$  through binding to stationary endogenous  $\text{Ca}^{2+}$  buffers, we solve a finite difference approximation to a set of reaction-diffusion equations of the following form (Stern, 1992a; Wagner and Keizer, 1994):

$$\frac{\partial[\text{Ca}^{2+}]}{\partial t} = D_C \nabla^2[\text{Ca}^{2+}] + J_{\text{dye}} + J_{\text{buffers}} + J_{\text{pump}} + J_{\text{leak}} + J_{\text{ryr}} \quad (2)$$

$$\frac{\partial[\text{CaF}]}{\partial t} = D_F \nabla^2[\text{CaF}] - J_{\text{dye}} \quad (3)$$

$$\frac{\partial[\text{CaB}_n]}{\partial t} = -J_n \quad (4)$$

where  $D_F$  and  $D_C$  are the diffusion coefficients for the indicator dye and free  $\text{Ca}^{2+}$  (all the endogenous buffers are assumed to be immobile; see below) and  $J_{\text{buffers}}$  in Eq. 2 are given by  $J_{\text{buffers}} = \sum_n J_n$ . The various fluxes ( $J_{\text{dye}}$ ,  $J_{\text{buffers}}$ ,  $J_{\text{pump}}$ ,  $J_{\text{leak}}$ , and  $J_{\text{ryr}}$ ) are detailed below along with comments on our choice of parameter values (see Tables 1 and 2).

### Flux due to $\text{Ca}^{2+}$ release via the RyR ( $J_{\text{ryr}}$ )

In most simulations presented here, we model  $\text{Ca}^{2+}$  release from the SR as originating at a virtual point source rather than an extended release site (Langer and Peskoff, 1996; Blatter et al., 1997); that is,  $J_{\text{ryr}} = \sigma_{\text{ryr}} \delta(\vec{r})$ , where  $\sigma_{\text{ryr}}$  is the time-dependent source strength (in micromoles per second) and  $\delta(\vec{r})$ , the Dirac delta function, is a sharply peaked function indicating the focal release of  $\text{Ca}^{2+}$  at the origin (Smith et al., 1996). The standard form of  $\sigma_{\text{ryr}}$  (see Table 1) is equivalent to a 10-ms pulse of 2 pA amplitude injected into an infinite medium; however, the simplicity of the model allows a range of source strengths and duration to be explored. Results were also obtained for  $\text{Ca}^{2+}$  release from extended sources (see Fig. 9 and related text).

### The free $\text{Ca}^{2+}$ diffusion coefficient

The diffusion coefficient for free  $\text{Ca}^{2+}$  ( $D_C$ ) in aqueous solution of physiological ionic strength has been estimated to be 700–780  $\mu\text{m}^2/\text{s}$  (Wang, 1953). The value for diffusion of ions or uncharged molecules inside cytosol is usually reduced by a factor of 2–2.5, presumably due to tortuosity (i.e., obstacles force diffusion to follow a convoluted route) as well as increased viscosity. Values used in previous models range from 100  $\mu\text{m}^2/\text{s}$  (Langer and Peskoff, 1996) to 600  $\mu\text{m}^2/\text{s}$  (Pratusевич and Balke, 1996). We used a free  $\text{Ca}^{2+}$  diffusion coefficient of 250  $\mu\text{m}^2/\text{s}$  as our standard parameter value for  $D_C$ .

*Fluxes due to  $\text{Ca}^{2+}$  indicator dye and endogenous stationary buffers ( $J_{\text{dye}}$  and  $J_{\text{buffers}}$ )*

The fluxes for the indicator dye and each endogenous buffer take similar forms:

$$J_{\text{dye}} = -k_{\text{F}}^{+}[\text{Ca}^{2+}][\text{F}]_{\text{T}} - [\text{CaF}] + k_{\text{F}}^{-}[\text{CaF}] \quad (5)$$

$$J_{\text{n}} = -k_{\text{n}}^{+}[\text{Ca}^{2+}][\text{B}_{\text{n}}]_{\text{T}} - [\text{CaB}_{\text{n}}] + k_{\text{n}}^{-}[\text{CaB}_{\text{n}}] \quad (6)$$

In the first of these equations,  $[\text{F}]_{\text{T}}$  is the total concentration of indicator dye, and  $k_{\text{F}}^{+}$  and  $k_{\text{F}}^{-}$  are association and dissociation rate constants. Because we assume that the diffusion constant of the indicator dye is not affected by the binding of  $\text{Ca}^{2+}$ , and that the initial concentration profile of the indicator is uniform, the concentration profiles of  $\text{Ca}^{2+}$ -free indicator dye are given at all times by  $[\text{F}] = [\text{F}]_{\text{T}} - [\text{CaF}]$  (Wagner and Keizer, 1994). Similarly, for each component of the sum that defines  $J_{\text{buffers}}$ ,  $[\text{B}_{\text{n}}]_{\text{T}}$  is the total concentration of buffer  $n$ ;  $k_{\text{n}}^{+}$  and  $k_{\text{n}}^{-}$  are association and dissociation rate constants; and the concentration of free buffer binding sites is taken to be  $[\text{B}_{\text{n}}] = [\text{B}_{\text{n}}]_{\text{T}} - [\text{CaB}_{\text{n}}]$ .

*Endogenous  $\text{Ca}^{2+}$  buffer parameters.* Table 2 summarizes our knowledge of endogenous  $\text{Ca}^{2+}$  buffers in cardiac myocytes on the basis of biochemical measurement (for a review see Bers, 1991) and functional studies (Sipido and Wier, 1991). Those buffers possessing specific  $\text{Ca}^{2+}$  binding sites include calmodulin and the contractile regulatory protein troponin C. Although they are less specific to  $\text{Ca}^{2+}$ , we include the phospholipid membranes of the sarcoplasmic reticulum (outer leaflet) and the sarcolemma (inner leaflet) as two additional  $\text{Ca}^{2+}$  buffers because the anion groups on the membrane surface constitute a low affinity, high capacity  $\text{Ca}^{2+}$  binding site (Bers et al., 1985; Post and Langer, 1992). These protein and membrane  $\text{Ca}^{2+}$  ligands were considered immobile in our model simulation.

*Indicator dye (fluo-3) parameters.* Though fluo-3 is unsuitable for two-wavelength ratiometric measurement of  $[\text{Ca}^{2+}]_{\text{i}}$ , it has been the indicator of choice for detecting  $\text{Ca}^{2+}$  sparks.  $\text{Ca}^{2+}$ -bound fluo-3 fluoresces  $\sim 200$  times more intensely than its  $\text{Ca}^{2+}$ -free counterpart (Harkins et al., 1993). This high  $F_{\text{max}}/F_{\text{min}}$  ratio results in high signal contrast and high signal-to-noise ratio, accounting in part for its superiority (in the context of detecting local  $[\text{Ca}^{2+}]_{\text{i}}$  elevations) over other widely used ratiometric  $\text{Ca}^{2+}$  indicators such as fura-2 and indo-1. In addition, the visible excitation wavelength (488 nm) of fluo-3 produces little autofluorescence and is expected to induce less photodamage in dye-loaded cells. Our  $\text{Ca}^{2+}$  spark model assumes that the fluorescence signal (in the absence of optical blurring) at a given spatial position is directly proportional to the local concentration of  $\text{Ca}^{2+}$ -bound indicator ( $[\text{CaF}]$ ).

Fluo-3 is a penta-valent anion (mol wt 765) and is predicted to have a diffusion coefficient of  $90 \mu\text{m}^2/\text{s}$  (Wang, 1953; Harkins et al., 1993). However, the apparent diffusion coefficient of fluo-3 measured in skeletal muscle fibers ranges only between 12 to  $30 \mu\text{m}^2/\text{s}$  (Harkins et al., 1993), suggesting that 80% of the indicator (or equivalently, an

individual dye molecule 80% of the time) is bound to immobile cellular constituents. Because of this and other experimental evidence that fluo-3 interacts with proteins of large molecular weight (e.g., aldolase; see Harkins et al., 1993), we have included fluo-3 immobilization in our model by either 1) partitioning the simulated indicator into two fractions, one stationary and one mobile, or 2) using a reduced, apparent diffusion coefficient for the indicator of  $20 \mu\text{m}^2/\text{s}$ . We use the second method here, a decision justified because it reduces the number of parameters needed to characterize fluo-3, easing the interpretation of our calculations. However, it should be noted that the accuracy of this method depends on indicator dye and endogenous buffer parameters. For example, the  $\text{Ca}^{2+}$  profile predicted by the steady-state rapid buffering approximation is given by an equation in which the diffusion coefficient and concentration of mobile buffer occur as a product (see Eq. 10 in Smith, 1996, where  $\varphi_j = D_j[\text{B}_j]_{\text{T}}K_j$ ). This implies that when buffer parameters are such that the rapid buffering approximation is valid, the simplified representation of fluo-3 transport is also accurate as time increases. However, given the moderate kinetics of fluo-3 used here, the validity of this approximation decreases in simulations that involve high concentrations of indicator dye (see Fig. 3).

Recent work indicates that the cytoplasmic environment also alters the interaction of the indicator with  $\text{Ca}^{2+}$ , markedly slowing both the dissociation rate [ $k_{\text{F}}^{-} = 200\text{--}700 \text{ s}^{-1}$  in solution (Eberhard and Erne, 1989) versus  $90 \text{ s}^{-1}$  inside skeletal muscle fiber (Harkins et al., 1993)] and the association rate [ $k_{\text{F}}^{+} = 80 \mu\text{M}^{-1}\text{s}^{-1}$  in vivo (Harkins et al., 1993) versus  $\sim 1000 \mu\text{M}^{-1}\text{s}^{-1}$  in vitro (Eberhard and Erne, 1989)]. Because the  $k_{\text{F}}^{+}$  and  $k_{\text{F}}^{-}$  are not equally affected, the dissociation constant ( $K_{\text{F}}$ ) of fluo-3 for  $\text{Ca}^{2+}$  is increased from  $0.4 \mu\text{M}$  to nearly  $1\text{--}3 \mu\text{M}$  (Harkins et al., 1993). The exact cause for these changes is unclear. These effects were included in the model through our choice of reduced association ( $k_{\text{F}}^{+} = 80 \mu\text{M}^{-1}\text{s}^{-1}$ ) and dissociation ( $k_{\text{F}}^{-} = 90 \text{ s}^{-1}$ ) rates for fluo-3 in our reference parameter set (see Table 2). It should be noted that if the changes in the interaction of the dye with calcium in the cytoplasmic environment are due to the same binding that reduces the apparent diffusion coefficient of the dye, our assumption that the diffusion coefficient is independent of calcium binding may be violated. For simplicity, such effects were not considered here.

*Flux due to  $\text{Ca}^{2+}$ -ATPases ( $J_{\text{pump}}$ ) and passive leak ( $J_{\text{leak}}$ )*

$\text{Ca}^{2+}$  resequestration by  $\text{Ca}^{2+}$  ATPases located in the SR membrane is a component of the model. The turnover rate as a function of instantaneous, local  $[\text{Ca}^{2+}]_{\text{i}}$  is (Bassani et al., 1994)

$$J_{\text{pump}} = \frac{v_{\text{pump}}^{\text{max}}[\text{Ca}^{2+}]_{\text{i}}^m}{K_{\text{pump}}^m + [\text{Ca}^{2+}]_{\text{i}}^m}, \quad (7)$$

where  $K_{\text{pump}}$  is  $184 \text{ nM}$ ,  $m$  is  $3.98$ , and  $v_{\text{pump}}^{\text{max}}$  is  $208 \mu\text{Ms}^{-1}$ . The contribution of SL  $\text{Na}^{+}/\text{Ca}^{2+}$  exchanger is ignored

because of its minor role in regulating cellular  $[Ca^{2+}]_i$  transients in rat ventricular myocytes (Balke et al., 1994). Because we do not explicitly keep track of the concentration of  $Ca^{2+}$  in the SR, the model requires an SR leak to balance  $J_{pump}$  when  $Ca^{2+}$  is at the background concentration ( $c_\infty = 0.1 \mu M$ ). The magnitude of the SR leak is thus constant and given by

$$J_{leak} = -J_{pump}(c_\infty) = -\frac{V_{pump}^{max} c_\infty^m}{K_{pump}^m + c_\infty^m}. \quad (8)$$

#### Optical blurring: the point spread function

The light microscopic image of a dimensionless optical point, the so-called point spread function (PSF), extends in three dimensions and is elongated along the optical axial direction. Although confocal modality is designed to reduce axial as well as lateral blurring, a confocal image is never blur-free. Reported confocal PSFs have an axial full width at half-maximum (FWHM) of 0.7–1.4  $\mu m$  and lateral FWHM of  $\sim 0.4 \mu m$  (e.g., Cheng et al., 1993; Pratusевич and Balke, 1996), comparable to the dimensions of a  $Ca^{2+}$  spark. Thus, we have taken optical blurring into account in these simulations. Our model PSF,  $G(x, y, z)$ , is a 3-D Gaussian function having axial (FWHM<sub>z</sub>) and lateral (FWHM<sub>xy</sub>) full width at half-maximum of 0.8  $\mu m$  and 0.4  $\mu m$ , respectively

$$G(x, y, z) = g(x, \sigma_{xy})g(y, \sigma_{xy})g(z, \sigma_z) \quad (9)$$

where  $g(w, \sigma) = (2\pi\sigma)^{-1/2} \exp(-w^2/2\sigma)$  and  $\sigma_{xy}$  and  $\sigma_z$  are related to the FWHM in the axial and lateral directions through  $g(\text{FWHM}/2) = g(0)/2$ , that is,  $\sigma_{xy} = (0.4 \mu m)^2/(8 \ln 2)$  and  $\sigma_z = (0.8 \mu m)^2/(8 \ln 2)$ . Thus, in our calculations, the value of simulated fluorescence at any given position is given by a numerical approximation to the convolution of the simulated dye profile with the model PSF given above

$$[CaF]_{avg}(x; Y_{offset}, Z_{offset}) = \iiint [CaF](x', y', z') G(x - x', Y_{offset} - y', Z_{offset} - z') dx' dy' dz' \quad (10)$$

where the integral is taken over the simulation volume. The parameters  $Y_{offset}$  and  $Z_{offset}$  represent the degree to which the origin of the spark is out of register with the center of the PSF, while  $x$  is the distance along the line scan. In this manuscript, simulation results are often reported as  $F/F_0$ , by which we mean  $[CaF]_{avg}/[CaF]_\infty$ , where  $[CaF]_\infty$  is the resting fluorescence, i.e., the concentration of CaF when the dye is in equilibrium with the background  $Ca^{2+}$  concentration

$$[CaF]_\infty = \frac{c_\infty [F]_T}{K_F + c_\infty}. \quad (11)$$

#### Implementation of model

The finite difference scheme used to numerically solve Eqs. 2–8 is presented in the Appendix. In its simplest form, the model components (e.g., exogenous  $Ca^{2+}$  buffers, indicator dye, and SR  $Ca^{2+}$ -ATPases) are assumed to be homogeneously distributed in the cytosol, diffusion of mobile molecules is isotropic, and the  $Ca^{2+}$  release responsible for the  $Ca^{2+}$  spark defines the origin of a spherical polar coordinate system. Under these conditions, all concentration profiles are spherically symmetric throughout the simulation. Because of its simplicity and computational efficiency, spherical symmetry is assumed in many of the simulations presented here. However, even in these “radial” simulations, the model PSF is anisotropic, so calculations for optically blurred sparks off-center in the axial direction ( $Z_{offset} > 0$ ,  $Y_{offset} = 0$  in Eq. 10) are different from sparks off-center in the transverse direction ( $Y_{offset} > 0$ ,  $Z_{offset} = 0$ ).

Some anisotropies in  $Ca^{2+}$  sparks have been attributed to cellular structure and anisotropic diffusion (Cheng et al., 1996b; Parker et al., 1996) rather than imaging. To investigate the effects of inhomogeneously distributed  $Ca^{2+}$ -ATPases and  $Ca^{2+}$ -binding proteins, anisotropic diffusion of  $Ca^{2+}$  ions and indicator, and release from an extended source of  $Ca^{2+}$ , we have also implemented a simulation using a cylindrical (i.e., an axisymmetric) coordinate system, where  $r$  represents the distance from a  $Ca^{2+}$  release site in the transverse direction (parallel to the plane of a Z-line) and  $z$  represents the longitudinal distance (perpendicular to the plane of a Z-line) from the origin of the  $Ca^{2+}$  spark. The finite difference scheme described in the Appendix is a description of our numerical implementation of this model. The spherically symmetric simulation is easily derived from it.

In both the radial and cylindrical simulations, the initial condition for  $Ca^{2+}$  is a uniform background concentration ( $[Ca^{2+}] = c_\infty = 0.1 \mu M$ ). At the beginning of the simulation, endogenous  $Ca^{2+}$  buffers and exogenous indicator dye are in equilibrium with  $Ca^{2+}$ . These concentrations are also used in a Dirichlet (absorbing) boundary condition for each variable distant from the  $Ca^{2+}$  release site, that is, at  $r = R_{max}$  and  $z = Z_{max}$ . Thus, in locations where the source has no effect, the solution is required to be in equilibrium with  $Ca^{2+}$  at all times (see p. 7, Morton and Mayers, 1994). In all calculations,  $R_{max}$  and  $Z_{max}$  are  $> 10 \mu m$ , a value large enough that this choice does not influence the numerical results.

## EXPERIMENTAL METHODS

### Confocal immunofluorescence imaging

Single cells were prepared from rat hearts using a standard method (Cheng et al., 1993). After isolation, the cells were resuspended in normal extracellular saline solution and allowed to settle into a soft pellet. The cells were resuspended in  $-20^\circ C$  ethanol to fix and permeabilize them and then processed for immunofluorescence (Kieval et al., 1992). The cells were exposed to a rabbit primary antibody to the SR  $Ca^{2+}$  ATPase and then treated with an FITC-labeled goat anti-rabbit antibody. We used a Zeiss LSM-410 microscope to image the immunolocalization of the SR  $Ca^{2+}$



ATPase in the cells (see Fig. 6). The sarcomeric distribution of the enzyme was assumed to be proportional to the fluorescence intensity in the confocal section. The final distribution pattern was a signal-averaged image of the distribution around the Z-line.

### Other experimental methods

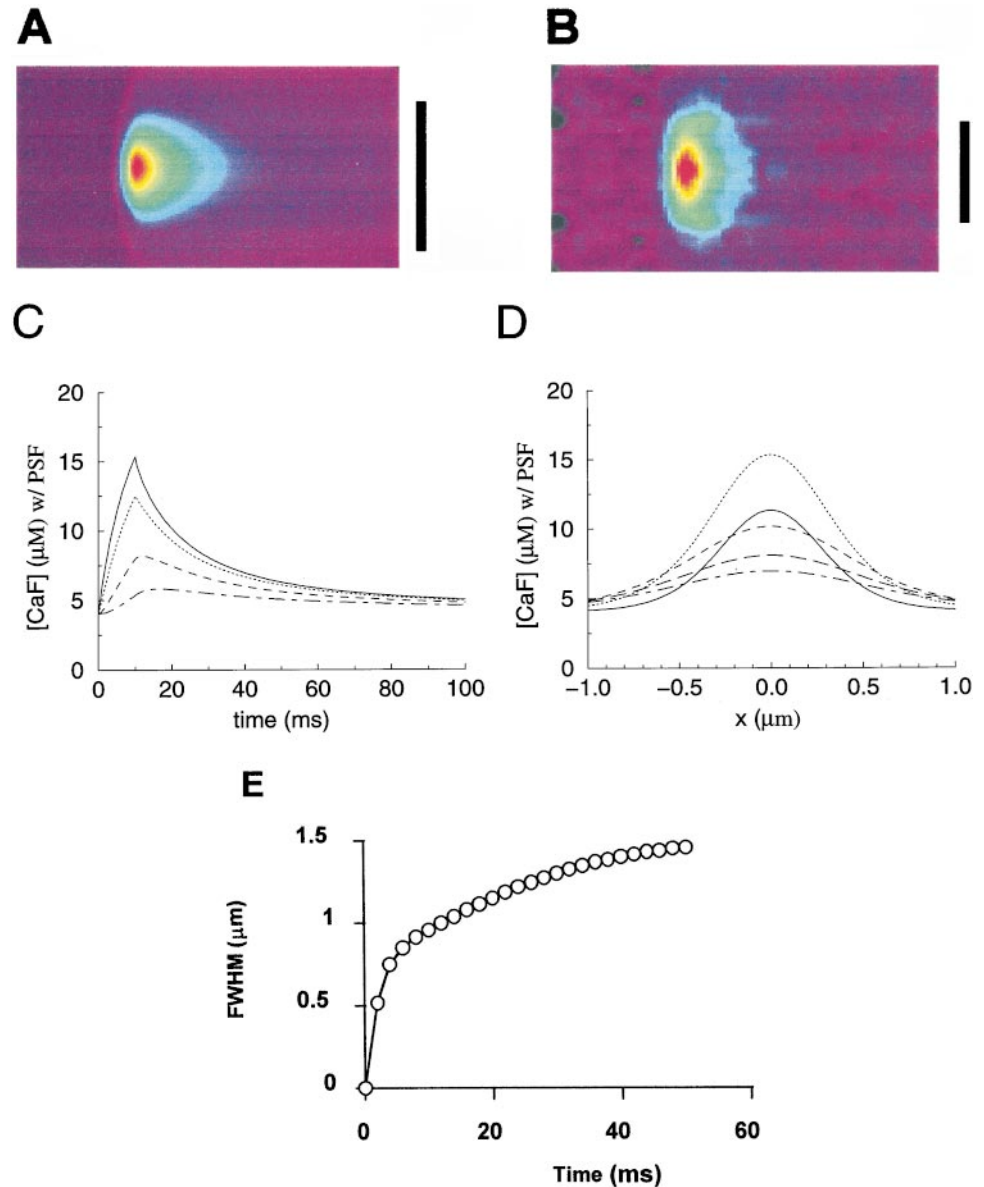
Single ventricular myocytes were isolated from adult Sprague-Dawley rats (2–3 months old, weight 225–300 g) using standard enzymatic techniques, as reported previously (Xiao et al., 1997). Cells were loaded with the  $\text{Ca}^{2+}$  indicator by incubation with 10  $\mu\text{M}$  Fluo-3 AM (Molecular Probes, Eugene, OR) for 12 min and then stored in HEPES buffer solution containing (in mM) 137 NaCl; 5.4 KCl; 1.2  $\text{MgCl}_2$ ; 1.2  $\text{NaH}_2\text{PO}_4$ ; 1  $\text{CaCl}_2$ ; 10 glucose and 20 Hepes (pH 7.4). Confocal imaging of spontaneous  $\text{Ca}^{2+}$  sparks was performed using a Zeiss LSM-410 inverted confocal microscope (Carl Zeiss, Inc., Germany) at a pixel width of 0.15  $\mu\text{m}$  and a scan rate of 2.0 ms per line. The axial and radial resolutions of the imaging system were 0.9 and 0.4  $\mu\text{m}$ , respectively. Image data were analyzed using IDL software (Research Systems, Boulder, CO). All experiments were conducted at room temperature (21–23°C).

## RESULTS

### $\text{Ca}^{2+}$ flux underlying elementary $\text{Ca}^{2+}$ release events

Fig. 1 A shows a space-time plot of a simulated “ $\text{Ca}^{2+}$  spark” produced by a 2 pA, 10 ms local  $\text{Ca}^{2+}$  release, as observed along a line placed 500 nm laterally from the release origin, with the PSF depicted in Eq. 9. For comparison, experimental data of an average  $\text{Ca}^{2+}$  spark from a rat ventricular myocyte are displayed in panel B. Sample traces of time courses and spatial profiles of the simulated spark are shown in panels C and D, respectively. When the simulated linescan was directly aligned with the spark center (not shown), normalized peak fluorescence,  $F/F_0$ , was as high as 3.76, similar to the brightest sparks seen in cells (Song et al., 1997; Blatter et al., 1997). As the scan line moved radially away from the center, the simulated peak

**FIGURE 1** Properties of model  $\text{Ca}^{2+}$  spark. (A) Simulated and (B) experimental linescan image of  $\text{Ca}^{2+}$  sparks. To produce the image in panel B, 12 sparks from rat ventricular myocytes are aligned and averaged twice by adding their original images and their spatially reversed images. Scale bars: 2  $\mu\text{m}$ . Time: 200 ms from left to right. (C) Simulated confocal spot recording of time courses of the model  $\text{Ca}^{2+}$  spark at different degrees of offset. From top to bottom,  $Y_{\text{offset}} = 0.0, 0.25, 0.5, \text{ and } 0.75 \mu\text{m}$ ;  $Z_{\text{offset}}$  is zero. (D) Fluorescence ( $[\text{CaF}]$ ) profiles at five different times after the beginning of an in-focus ( $Y_{\text{offset}} = Z_{\text{offset}} = 0.0 \mu\text{m}$ )  $\text{Ca}^{2+}$  release event which occurs at  $t = 0$ . In ms:  $t = 5$  (solid line), 10 (dotted line), 20 (dashed line), 30 (long-dashed line), and 40 (dot-dashed line). (E) Spark breadth (FWHM) as a function of time. For simulations in panels A and E,  $Y_{\text{offset}} = 0.5 \mu\text{m}$  and  $Z_{\text{offset}} = 0$ . All other parameters used are listed in Tables 1 and 2. After  $\text{Ca}^{2+}$  release terminates ( $t > 10$  ms), the time course of the square of the FWHM gives an apparent diffusion coefficient for  $\text{Ca}^{2+}$  of 31  $\mu\text{m}^2/\text{s}$  (not shown).



amplitude was reduced while the time to peak was blunted and the decay time was increased (Fig. 1 *C*). At the representative distance shown ( $Y_{\text{offset}} = 0.5 \mu\text{m}$ ), the peak  $F/F_0$  was 2.01, the half decay time ( $T_{1/2}^{\text{decay}}$ ) was 25.3 ms, and the FWHM was  $0.89 \mu\text{m}$  at time of peak  $F/F_0$  ( $t = 12 \text{ ms}$ ). Panels *D* and *E* show that the spread of the fluorescence in space exhibited two phases: a rapid initial expansion, rendering the flattened head of the comet-shaped spark in the linescan image (panels *A* and *B*), followed by a progressive growth that reached a FWHM of  $1.40 \mu\text{m}$  at 30 ms after release was terminated (panel *E*).

Experimentally, the local increase of fluorescence of a  $\text{Ca}^{2+}$  spark is  $\sim 2.0$  and the time constant of decay is around 20 ms (Fig. 1 *B*). The amplitude and rates of rise and decline of the simulated  $\text{Ca}^{2+}$  spark are thus comparable with the experimental data. However, the FWHM of the model spark is only half that observed experimentally ( $1.7\text{--}2.2 \mu\text{m}$ , Cheng et al., 1993; López-López et al., 1995; see below). Thus all the salient measures of  $\text{Ca}^{2+}$  sparks (with the exception of FWHM) can be readily reproduced by the radial model using a  $\text{Ca}^{2+}$  flux resembling unitary RyR current seen in lipid bilayer [ $\sim 2 \text{ pA}$  at 0 mV and 2.4 mM SR luminal  $\text{Ca}^{2+}$  (Tinker et al., 1993); 5.4–22.3 ms mean open time in the presence of ATP and 0.1  $\mu\text{M}$  cytosolic  $\text{Ca}^{2+}$  and pCa 0.48–2.0 on the luminal side (Lukyanenko et al., 1996)]. This is consistent with the notion that  $\text{Ca}^{2+}$  sparks arise from single RyR channel openings; however, it is also compatible with the multiple-channel hypothesis of spark origin if the RyR in vivo has a reduced conductance

or if RyR-RyR interaction is required to provide a longer effective mean open time (see below).

### Physiological determinants of $\text{Ca}^{2+}$ spark properties

Identifying cellular and molecular features involved in the shaping of  $\text{Ca}^{2+}$  spark properties is essential not only to understanding physiological modulation of elementary  $\text{Ca}^{2+}$  signaling, but also to integrating data in various tissues and species, and to devising strategies to experimentally manipulate SR  $\text{Ca}^{2+}$  release at the elementary level. To this end, model simulation can be exploited to gain insights that may not be easily obtained with experiment (e.g., dissecting contributions from each of the  $\text{Ca}^{2+}$  handling mechanisms). Starting from the standard parameter set described in Tables 1 and 2, we systematically varied model parameters (e.g., source strength and duration, the abundance of endogenous  $\text{Ca}^{2+}$  buffers, and the maximum rate of  $\text{Ca}^{2+}$  resequestration) over several orders of magnitude and studied subsequent changes in the properties of simulated  $\text{Ca}^{2+}$  sparks. Additional simulations with variable dye properties, spatial inhomogeneities, anisotropy, and spatially extended sources are deferred to later sections.

#### Spark brightness (peak $F/F_0$ )

As expected, the amplitude or “brightness” of a simulated  $\text{Ca}^{2+}$  spark was very sensitive to the magnitude of the  $\text{Ca}^{2+}$

**TABLE 1 Model parameters**

Parameter	Definition	Standard Value
Local $\text{Ca}^{2+}$ release from the SR		
$i_{\text{Ca}}$	Amplitude of elemental $\text{Ca}^{2+}$ release	2 pA
$F$	Faraday's constant	96500 C/mol
$Z$	Valence of $\text{Ca}^{2+}$ ion	2
Diffusion of free $\text{Ca}^{2+}$ and fluo-3		
$D_{\text{C}}$	Diffusion coefficient of free $\text{Ca}^{2+}$ in cytosol	$250 \mu\text{m}^2/\text{s}$
$D_{\text{F}}$	Diffusion coefficient of fluo-3 and $\text{Ca}^{2+}$ -fluo-3 in cytosol	$20 \mu\text{m}^2/\text{s}$
fluo-3		
$[F]_{\text{T}}$	Total concentration of fluo-3 (see Table 2)	
$k_{\text{F}}^+$	Association rate constant for $\text{Ca}^{2+}$ binding to fluo-3	
$k_{\text{F}}^-$	Dissociation rate constant of $\text{Ca}^{2+}$ from fluo-3	
$K_{\text{F}}$	$= k_{\text{F}}^-/k_{\text{F}}^+$	
$\text{Ca}^{2+}$ resequestration by SR $\text{Ca}^{2+}$ -ATPases		
$v_{\text{pump}}^{\text{max}}$	Maximum rate of $\text{Ca}^{2+}$ reuptake	$208 \mu\text{M}/\text{s}$
$K_{\text{pump}}$	Michaelis constant	$0.184 \mu\text{M}$
$m$	Hill coefficient	3.9
$\text{Ca}^{2+}$ Buffering (see Table 2)		
$[B_{\text{n}}]_{\text{T}}$	Total concentration for each $\text{Ca}^{2+}$ buffer	
$k_{\text{n}}^+$	Association rate constant for $\text{Ca}^{2+}$ binding	
$k_{\text{n}}^-$	Dissociation rate constant of $\text{Ca}^{2+}$ from ligand	
$K_{\text{n}}$	$= k_{\text{n}}^-/k_{\text{n}}^+$	
$c_{\infty}$	Intracellular free $\text{Ca}^{2+}$ concentration at rest	100 nM
PSF of confocal microscope		
$\text{FWHM}_z$	Axial full width at half-maximum	$0.8 \mu\text{m}$ ( $\sigma_z = 0.115 \mu\text{m}^2$ )
$\text{FWHM}_{xy}$	Lateral full width at half-maximum	$0.4 \mu\text{m}$ ( $\sigma_{xy} = 0.0289 \mu\text{m}^2$ )

**TABLE 2** Dye and endogenous  $\text{Ca}^{2+}$  buffers

$\text{Ca}^{2+}$ Buffer	$k_n^+$ ( $\mu\text{M}^{-1}\text{s}^{-1}$ )	$k_n^-$ ( $\text{s}^{-1}$ )	$[B_n]_T$ ( $\mu\text{M}$ )	$K_n$ ( $\mu\text{M}$ )
Fluo-3	80	90	50	1.13
Calmodulin	100	38	24	0.38
Troponin C	39	20	70	0.51
SR membrane	115	100	47	0.87
SL membrane	115	1000	1124	8.7

source (Fig. 2 *B*). For  $\text{Ca}^{2+}$  fluxes of 0.5–4.0 pA, peak  $F/F_0$  varied nearly in proportion to the source strength (Fig. 2 *B*). Thus, under these conditions, the fluorescence signal is not saturated (see also Fig. 3 *E*), even though the local  $\text{Ca}^{2+}$  concentration (Stern, 1992a,b; Langer and Peskoff, 1996; Soeller and Cannell, 1997; see below) is expected to be much greater than the dissociation constant of fluo-3 ( $K_F = 1.13 \mu\text{M}$ ). This occurs because the indicator and free  $\text{Ca}^{2+}$  are not at equilibrium during the spark event. Additionally, the minimal detection volume, or “voxel” ( $\sim 0.13 \mu\text{m}^3$ ) is larger than the microdomain of saturating  $\text{Ca}^{2+}$  (see below). Indeed, recent experimental data show that depletion of SR  $\text{Ca}^{2+}$  reduced spark amplitude (Sato et al., 1997; Song et al., 1997) and that the reduced amplitude is linearly corre-

lated with the caffeine-releasable SR  $\text{Ca}^{2+}$  load (Song et al., 1997). Thus, both theory and experiment reinforce the idea that changes in spark amplitude can result from changes in the underlying  $\text{Ca}^{2+}$  flux.

The intensity of the simulated fluorescence signal depends also on the release duration. Given a long-lasting  $\text{Ca}^{2+}$  flux of 2 pA, the local fluorescence signal did not reach its peak level until  $\sim 50$  ms elapsed (Fig. 2 *A*). It takes time both to “load” the endogenous  $\text{Ca}^{2+}$  buffer and for the dye to follow the free  $\text{Ca}^{2+}$  change. Hence, changes in the duration of  $\text{Ca}^{2+}$  release can alter spark amplitude. This result indicates that interpretation of optically measured spark amplitude is equivocal, in contrast with electrophysiological measurement of channel currents. Furthermore, this finding may also help to resolve a paradoxical observation that a skeletal muscle spark is  $\sim 3$  (Klein et al., 1996) or 5–10 times (based on “noise analysis” and in the presence of 10 mM exogenous mobile buffer, EGTA) (Tsugorka et al., 1995) smaller in amplitude than a cardiac spark, despite the fact that cardiac and skeletal RyR’s are closely related isoforms. This calculation suggests that the difference might reside in a tissue-dependent open duration for in vivo gating of RyR.

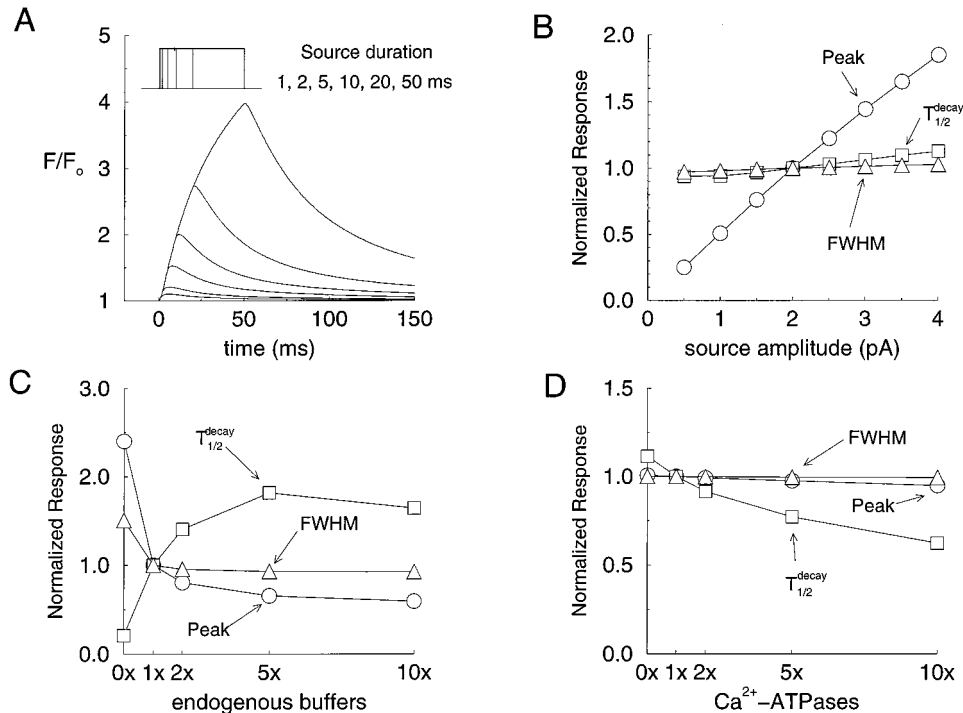


**FIGURE 2** Parameter sensitivity study revealing the determinants of spark size, amplitude, and kinetics. (A) Duration of  $\text{Ca}^{2+}$  release. A family of time courses for the square pulse of 2 pA amplitude and duration of 1, 2, 5, 10, 20, or 50 ms are shown in the inset. Even at 50 ms the fluorescence signal has not reached the steady state. (B) Source amplitude is varied from 0.5 to 4.0 pA for a square pulse of 10 ms duration. The values of peak (circles), FWHM (triangles), and half-time of decay (squares) are plotted for each source strength, normalized to the value for our standard source strength, which was 2 pA. The numerical values for 2 pA are  $[\text{CaF}] = 8.20 \mu\text{M}$  at peak, a FWHM =  $0.89 \mu\text{m}$ , and a half-time of decay of 25.3 ms. Note that sensitivity to the source amplitude is peak  $\gg T_{1/2}^{\text{decay}} > \text{FWHM}$ . (C) Concentration of endogenous buffers is varied so that they are all either absent (0x) or at 1x, 2x, 5x, or 10x their standard concentrations (see Table 2). Normalized peak (circles), FWHM (triangles), and half-time of decay (squares) are plotted. (D) Maximum turnover rate of the SR  $\text{Ca}^{2+}$ -ATPases is varied, and normalized peak (circles), FWHM (triangles), and half-time of decay (squares) are plotted. SR pumps, even at 10 times their standard value, have little effect on peak or FWHM, and only a small effect on the half-time of decay. For all simulations,  $Y_{\text{offset}} = 0.5 \mu\text{M}$ ,  $Z_{\text{offset}} = 0$ .

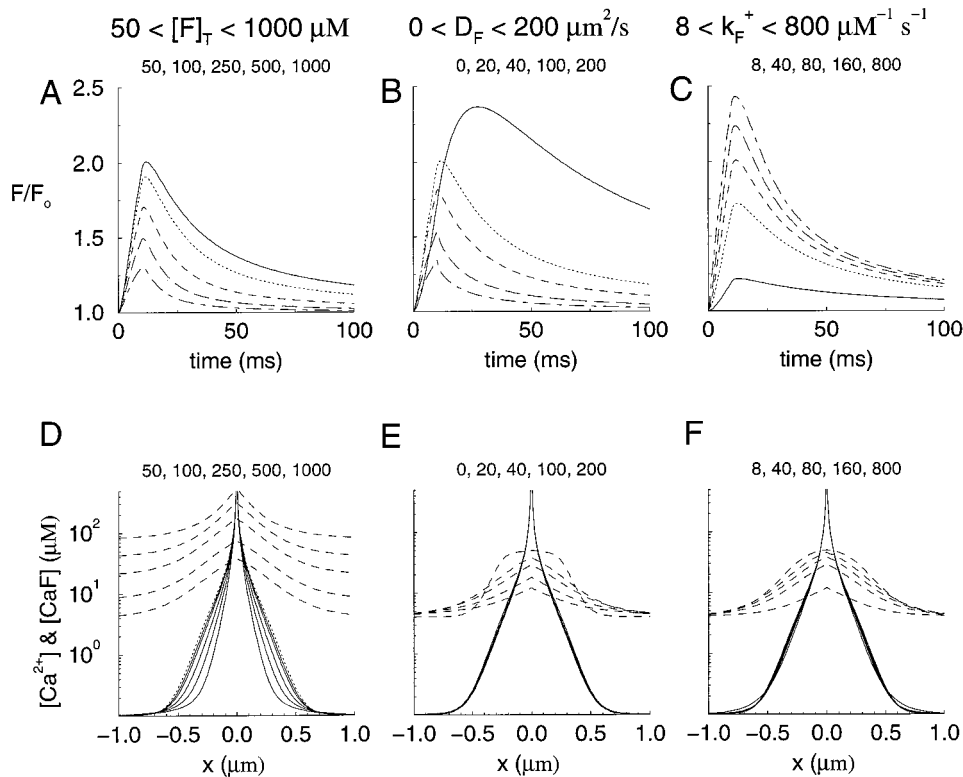


FIGURE 3 Effects of indicator dye parameters on spark properties. (A–C) Simulated time course of normalized, blurred fluorescence signal ( $F/F_0$ ), with  $Y_{offset} = 0.5 \mu m$  and  $Z_{offset} = 0$ , and standard parameters (see Tables 1 and 2) unless otherwise noted. (A) Effect of variable amount of  $Ca^{2+}$  indicators. From top to bottom: total dye concentration ( $[F]_T$ ) is 50, 100, 250, 500, and 1000  $\mu M$ . Note that the  $F/F_0$  is greater when there is less indicator, indicating that the indicator is perturbing the  $Ca^{2+}$  profile (see panel D). (B) Effect of varying the mobility of the dye. From top to bottom,  $D_F$  takes values of 0 (immobile), 20, 40, 100, and 200  $\mu m^2/s$ . For stationary dye, note the marked differences in terms of amplitude, time to peak, and relaxation. (C) Effect of dye rate constants. From bottom to top, the  $Ca^{2+}$  association rate constant of the indicator is increased from 8 to 40, 80, 160, and 800  $\mu M^{-1} s^{-1}$  and the corresponding dissociation rate constants are 9, 45, 90, 180, and 900  $s^{-1}$ , rendering  $K_F$  unchanged. (D–F)  $[Ca^{2+}]$  (solid line or dotted line) and  $[CaF]$  (dashed lines) profiles at  $t = 10$  ms. Parameters identical to panels A–C, respectively, except that  $Y_{offset} = Z_{offset} = 0$ . (D) Uppermost  $CaF$  profile (dashed line) and lowermost  $Ca^{2+}$  profile (solid line) are from simulation with total dye concentration ( $[F]_T$ ) of 1000  $\mu M$ . Dotted line shows the  $Ca^{2+}$  profile with no fluo-3. (E) Uppermost  $CaF$  profile (dashed line) and uppermost  $Ca^{2+}$  profile (solid line) are from simulation with immobile indicator ( $D_F = 0 \mu m^2/s$ ). (F) Uppermost  $CaF$  profile (dashed line) and lowermost  $Ca^{2+}$  profile (solid line) are from simulation with fastest dye kinetics ( $k_F^+ = 800 \mu M^{-1} s^{-1}$  and  $k_F^- = 900 s^{-1}$ ).

Varying the amount of endogenous stationary  $Ca^{2+}$  buffer had a moderate effect on spark amplitude (Fig. 2 C). Peak  $F/F_0$  decreased by  $\sim 30\%$  in the presence of 10-fold more  $Ca^{2+}$  buffer and increased by 2.4-fold if all endogenous  $Ca^{2+}$  buffer was removed. This suggests that variations in intracellular  $Ca^{2+}$ -buffering capacity, as well as release flux and duration, may contribute to the difference in  $Ca^{2+}$  spark amplitudes across cell type. Interestingly, the SR  $Ca^{2+}$  ATPase, whether totally inactive or enhanced by an order of magnitude in our simulations, had virtually no effect on spark amplitude (Fig. 2 D). This is in good agreement with the recent observation that spark amplitude is unchanged when SR  $Ca^{2+}$  ATPase activity was either abolished by thapsigargin or stimulated via  $\beta$ -adrenergic-mediated signal transduction (Gómez et al., 1996).

#### Spark decay time ( $T_{1/2}^{decay}$ )

The half-time of decay,  $T_{1/2}^{decay}$ , for  $Ca^{2+}$  sparks ( $\sim 20$  ms in cardiac myocytes) is strongly affected by both endogenous

$Ca^{2+}$  buffers and indicator properties in our model simulations. With the standard parameter set, the model spark decay time is  $\sim 25$  ms (Fig. 1 C), while in simulations in which the  $Ca^{2+}$  indicator (50  $\mu M$ ) is the sole  $Ca^{2+}$ -binding species,  $T_{1/2}^{decay}$  is reduced to 4 ms (Fig. 2 C). In contrast, if only a trace amount of fluo-3 (0.1  $\mu M$ ) is added to endogenous buffers, the result is 38 ms. These calculations indicate that *interaction* between endogenous buffers and the dye is a major contributor to the decay rate of elevated local fluorescence; that is, after the cessation of RyR flux, stationary buffers exposed to high  $Ca^{2+}$  discharge and act as a source of free  $Ca^{2+}$ , slowing the decay of  $Ca^{2+}$ -bound indicator. However, this effect is not a simple monotonic function of the buffer concentration. The maximum  $T_{1/2}^{decay}$  shown in Fig. 2 C occurs in the presence of 5 rather than 10 times the standard concentration of endogenous buffer. Since buffer capacity alone can alter the decay rate more than an order of magnitude, it would be of interest for future study to correlate the decay rate with the abundance of physiological  $Ca^{2+}$  buffers in various cell types. Local  $Ca^{2+}$



clearance by the SR  $\text{Ca}^{2+}$  ATPase had a small but noticeable contribution to the decline of fluorescence signal (Fig. 2 D), as was observed experimentally (Gómez et al., 1996). Furthermore, the decay rate was dependent on both release duration ( $T_{1/2}^{\text{decay}} = 24\text{--}37$  ms in Fig. 2 A) and  $\text{Ca}^{2+}$  release amplitude ( $T_{1/2}^{\text{decay}} = 24\text{--}29$  ms in Fig. 2 B).

#### Spark width: the full width at half maximum (FWHM)

As discussed above, using our standard parameter set the radial model predicts a FWHM that is about half the observed spark diameter. An unexpected feature of these calculations is that normalized spark breadth is not a strong function of the source amplitude (see Fig. 2 B). Indeed, most of the perturbations depicted in Fig. 2 have little effect on the FWHM of the simulated sparks. Total removal of the endogenous buffers produced the largest FWHM ( $1.3\ \mu\text{m}$  at 10 ms), which is 50% larger than the standard value (Fig. 2 C) but still 30% smaller than a typical experimentally observed spark. Increasing stationary buffer capacity 10-fold decreased spark FWHM by only 8%. Varying  $\text{Ca}^{2+}$ -ATPase activity from  $0\times$  to  $10\times$  did not significantly decrease the FWHM. Spatially distributing  $\text{Ca}^{2+}$  release over a ring  $0.6\ \mu\text{m}$  in diameter, representing the entry of  $\text{Ca}^{2+}$  into the cytosol via the opening of a diad cleft, only slightly increased spark size (see Fig. 9 and related text). Even varying the dye parameters from the standard values listed in Tables 1 and 2, it is difficult to increase the FWHM of the model spark without simultaneously increasing its brightness beyond what is typically seen experimentally ( $F/F_0 \sim 2.0$ ). Using the radial, isotropic simulation with a point source for  $\text{Ca}^{2+}$  release, we were able to achieve a typical experimentally observed FWHM ( $1.6\ \mu\text{m}$  at 10 ms) while still maintaining  $F/F_0 \approx 2$ , but this required increasing both the PSF size and the source amplitude 3-fold ( $i_{\text{Ca}} = 6.0$  pA,  $\sigma_z = 0.346\ \mu\text{m}^2$ , and  $\sigma_{xy} = 0.087\ \mu\text{m}^2$ , giving FWHM<sub>z</sub> of  $2.4\ \mu\text{m}$  and FWHM<sub>xy</sub> of  $1.2\ \mu\text{m}$ ).

#### The role of the indicator dye in spark formation

As in our preliminary calculations (Smith et al., 1996), we find that the concentration and mobility of indicator can alter the decay rate of a  $\text{Ca}^{2+}$  spark event. Fig. 3 A shows that adding higher concentrations of indicator has the counterintuitive effect of reducing the peak  $F/F_0$  as well as accelerating the decay rate. Fig. 3, B and E demonstrate that varying the mobility of fluo-3 dramatically changes both the spatial and temporal properties of the fluorescent signal. When  $50\ \mu\text{M}$  fluo-3 is totally immobilized ( $D_F = 0$ ), the decay of fluorescence signal is extremely slow ( $T_{1/2}^{\text{decay}} = 72$  ms), and the peak fluorescence signal (at  $Y_{\text{offset}} = 0.5\ \mu\text{m}$  and  $Z_{\text{offset}} = 0$ ) increased by 18% (panel B, top curve) relative to the result obtained with  $D_F = 20\ \mu\text{m}^2/\text{s}$ . Furthermore, the fluorescence signal (at  $Y_{\text{offset}} = Z_{\text{offset}} = 0$ ,  $t = 10$  ms) saturated over a radius of  $\sim 300$  nm and then sharply declined toward basal level (panel E, top dashed line). A

higher diffusion coefficient reduces the peak  $F/F_0$  (panel B) and allows the fluorescence signal to respond more quickly to the termination of  $\text{Ca}^{2+}$  release ( $T_{1/2}^{\text{decay}} = 8$  ms at  $D_F = 200\ \mu\text{m}^2/\text{s}$ ). These results show that indicator dye with even small mobility (here  $20\ \mu\text{m}^2/\text{s}$ ) has behavior markedly distinct from that of a stationary version of the same dye. Thus, use of immobile dyes [e.g., conjugated to dextran beads or to membrane proteins (Horne and Meyer, 1997)] may have both advantages (e.g., brighter but not necessarily more confined in space) and disadvantages (e.g., distorted kinetics).

Fig. 3, C and F examine the effects of indicator kinetics at  $0.1\times$ ,  $0.5\times$ ,  $1\times$ ,  $2\times$ , and  $10\times$  the nominal rate of fluo-3 while holding  $K_F$  constant. The simulated peak fluorescence change as a function of these rates (with lateral distance  $Y_{\text{offset}} = 0.5\ \mu\text{m}$ ) is 1.22, 1.72, 2.01, 2.24, and 2.43, respectively; and  $T_{1/2}^{\text{decay}}$  is 49, 31, 25, 23, and 22 ms. These results indicate that, for a given dissociation constant ( $K_F$ ), rapid indicators lead to both brighter sparks and faster spark decay rates. In addition, these calculations show that in all cases,  $T_{1/2}^{\text{decay}}$  is not easily estimated from the  $\text{Ca}^{2+}$  dissociation time constant (i.e., 110, 22, 11, 5.5, and 1.1 ms); rather,  $\text{Ca}^{2+}$  fluxes from dye diffusion and discharge of the immobile endogenous buffer largely determine  $T_{1/2}^{\text{decay}}$ . Another simulation result that may be counterintuitive is that slow indicator dye rate constants can result in spatially restricted fluorescence signals (Fig. 3 F).

#### The indicator dye perturbs $\text{Ca}^{2+}$ signaling

We have used the radial  $\text{Ca}^{2+}$  spark simulation to examine the extent to which the presence of an indicator dye perturbs the free  $\text{Ca}^{2+}$  signal. In Fig. 3 D, the  $\text{Ca}^{2+}$  profile in the absence of fluo-3 (outermost dashed line for  $\text{Ca}^{2+}$ ) nearly overlaps the  $\text{Ca}^{2+}$  profile in the presence of  $50\ \mu\text{M}$  fluo-3, the estimated dye concentration in most spark experiments. This suggests that this concentration of indicator has a negligible effect on physiological  $\text{Ca}^{2+}$  signaling. However, as the amount of the dye increased to concentrations used in some recent studies ( $1\text{--}2$  mM, Wang et al., 1997), free  $\text{Ca}^{2+}$  in regions distant ( $>100$  nm) from the origin is suppressed in a dose-dependent manner, resulting in a spatially confined  $\text{Ca}^{2+}$  signal (Fig. 3 D). Conversely, the fluorescence signal broadens slightly with increasing dye concentrations (Fig. 3 D). These calculations suggest that  $\text{Ca}^{2+}$  coupling between the SL and the SR (which occurs on a distance scale of tens of nanometers) is unlikely to be affected by submillimolar concentrations of fluo-3, consistent with results using other  $\text{Ca}^{2+}$  chelators (Sham, 1997). Nevertheless, such concentrations of indicator may have a major effect on  $\text{Ca}^{2+}$  coupling between more distant sites, e.g., during sequential recruitment of release units and the propagation of  $\text{Ca}^{2+}$  waves (Parker et al., 1996; Cheng et al., 1996a; Lukyanenko et al., 1996).

An unexpected result of these calculations is that changing parameters other than the total dye concentration has little effect on the free  $\text{Ca}^{2+}$  profiles, as shown by the nearly

overlapping  $\text{Ca}^{2+}$  profiles in Fig. 3 *E* ( $D_F = 0\text{--}200\ \mu\text{m}^2/\text{s}$ ) and Fig. 3 *F* ( $k_F^+ = 8\text{--}800\ \mu\text{M}^{-1}\text{s}^{-1}$ ). Similar results were obtained for the time course of local  $[\text{Ca}^{2+}]$  transients (data not shown). These indicator dye properties, while largely determining the appearance of the fluorescence signal, do not dramatically influence the rate of free  $\text{Ca}^{2+}$  clearance (via facilitated diffusion) when the dye is present at low concentrations ( $50\ \mu\text{M}$  throughout Fig. 3, *E* and *F*). Taken together, these calculations illustrate a dilemma confronting spark measurement and interpretation: fluorescence signals may not faithfully reflect changes in the underlying  $\text{Ca}^{2+}$  signal (Fig. 3 *D*) and vice versa (Fig. 3, *D* and *F*; see Fig. 7 and below for more examples).

### What elevated fluorescence tells us about the $\text{Ca}^{2+}$ signal

A  $\text{Ca}^{2+}$  spark is the experimentally measured elevation in fluorescence signal. We are interested in whether or not the true free  $\text{Ca}^{2+}$  signal can be derived from the fluorescence signal after correcting for distortions due to optical blurring. As shown in Fig. 4 *A*, the simulated fluo-3 fluorescence profile ( $[\text{CaF}]$  w/PSF at  $Y_{\text{offset}} = Z_{\text{offset}} = 0$  and  $t = 10\ \text{ms}$ ,

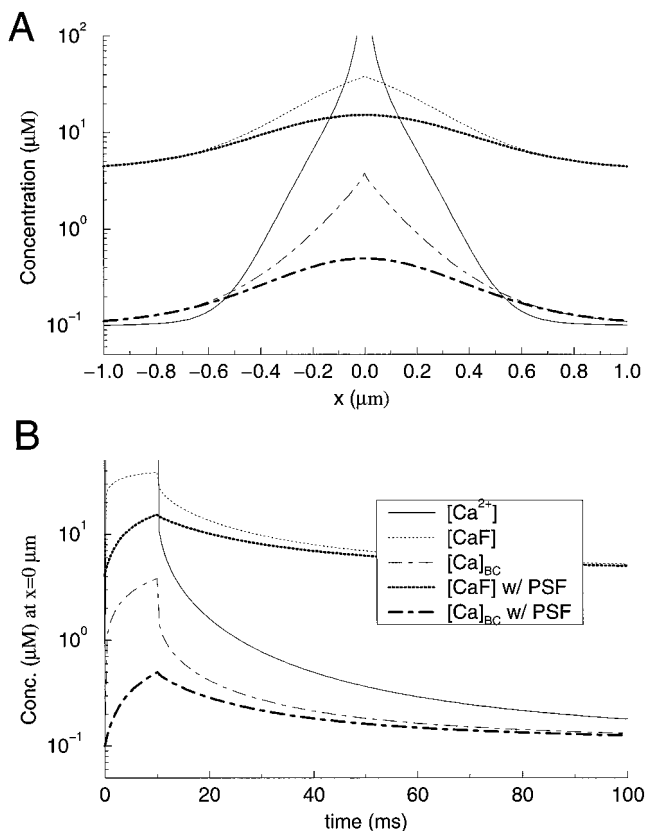


FIGURE 4 Back-calculation of  $[\text{Ca}^{2+}]$  from the fluorescence signal. (A) Simulated spatial profiles of  $[\text{Ca}^{2+}]$  (solid line),  $[\text{CaF}]$  (thin dotted line),  $[\text{CaF}]$  convolved with PSF (thick dotted line), and calculated  $[\text{Ca}^{2+}]$  using  $[\text{CaF}]$  with PSF (thick dot-dashed line) or  $[\text{CaF}]$  (thin dot-dashed line).  $Y_{\text{offset}} = Z_{\text{offset}} = 0$  and  $t = 10\ \text{ms}$ . (B) Time courses of these signals at  $x=0\ \mu\text{m}$ .  $Y_{\text{offset}} = Z_{\text{offset}} = 0$ .

heavy dotted line) is a poor representation of the  $\text{Ca}^{2+}$  profile (solid line), even in the absence of any out-of-focus blurring (light dotted line). Furthermore, the  $\text{Ca}^{2+}$  profile back-calculated from the usual equilibrium formula applied to the blurred (heavy dashed line) or non-blurred (light dashed line) fluorescence profile still differs markedly from the simulated  $\text{Ca}^{2+}$  profile. Specifically, the back-calculated profile grossly underestimates  $[\text{Ca}^{2+}]$  near the origin, whereas in regions farther away ( $>0.5\ \mu\text{m}$  in the example shown in Fig. 4), the fluorescence overestimates  $[\text{Ca}^{2+}]$ . Both errors are attributable to the lack of equilibrium of  $\text{Ca}^{2+}$  with the indicator and the presence of large gradients for  $\text{Ca}^{2+}$  and fluo-3 (in both  $\text{Ca}^{2+}$ -free and  $\text{Ca}^{2+}$ -occupied forms) (Smith et al., 1996).

Not only is the  $\text{Ca}^{2+}$  signal more confined in space, but it also decays much more rapidly than the fluorescence signal (Fig. 4 *B*, solid line versus dotted lines). Back-calculation assuming equilibrium between dye and  $\text{Ca}^{2+}$  (Fig. 4 *B*, dashed lines) underestimates the transient free  $\text{Ca}^{2+}$  elevation at origin of spark, both during release and after release has terminated. Fig. 4 demonstrates that by using the current generation of  $\text{Ca}^{2+}$  probes and confocal fluorescence technology, it is not possible to ascertain the true  $[\text{Ca}^{2+}]_i$  signal from fluorescence measurements without quantitative modeling. Caution should be exercised in interpreting spatiotemporal dynamics of local  $\text{Ca}^{2+}$  on the basis of fluorescence measurement alone.

### Spark statistics: intrinsic variance versus variance due to off-center sampling

Since both the confocal PSF and  $\text{Ca}^{2+}$  sparks have finite dimensions, sparks seen in line scan imaging include both in-focus and out-of-focus events, and to date no detection algorithm has been devised that can discriminate between them. However, simulations can help to reveal how random sampling may distort  $\text{Ca}^{2+}$  spark statistics. Although this question has been addressed previously (Pratusevich and Balke, 1996), our calculations can address whether the mobility of the indicator dye influences these conclusions. We are also interested in the relation between the apparent and the intrinsic spark statistics, a question which to our knowledge has not to date been examined.

$\text{Ca}^{2+}$  release sites in cardiac cells are concentrated around Z-lines and exhibit a quasi-periodicity of  $\sim 1.8\ \mu\text{m}$  in the longitudinal direction (Carl et al., 1995; Sun et al., 1995; Cheng et al., 1996a; Parker et al., 1996). However, no ultrastructural data show strict regularity in the transverse direction. The transverse regularity, if any, may not be in register over many sarcomeres, e.g., 30–50 sarcomeres typically surveyed in a single linescan image. Thus, it is reasonable to assume that  $\text{Ca}^{2+}$  sparks originate at sites distributed randomly and uniformly around the confocal scanline. Given this assumption, we systematically calculated spark parameters, including  $F/F_0$ , FWHM, and  $T_{1/2}^{\text{decay}}$ , as functions of the lateral ( $Y_{\text{offset}}$ ) and axial ( $Z_{\text{offset}}$ ) displace-

ment of the center of the PSF from the origin ( $o$ ) of our standard  $\text{Ca}^{2+}$  spark (Fig. 5 A). The results are summarized as surface plots shown in Fig. 5, B–D. In general, off-center sparks have smaller amplitudes compared to the in-focus sparks (Fig. 5 B) while spark width (Fig. 5 C) and duration

(Fig. 5 D) increases with larger  $Y_{\text{offset}}$  and  $Z_{\text{offset}}$ . If we further assume a detect threshold of peak  $F/F_0 = 1.25$  due to the presence of noise (Pratusevich and Balke, 1996; Song et al., 1997), Fig. 5, E–G show the expected parametric distributions of a stereotyped event after random sampling

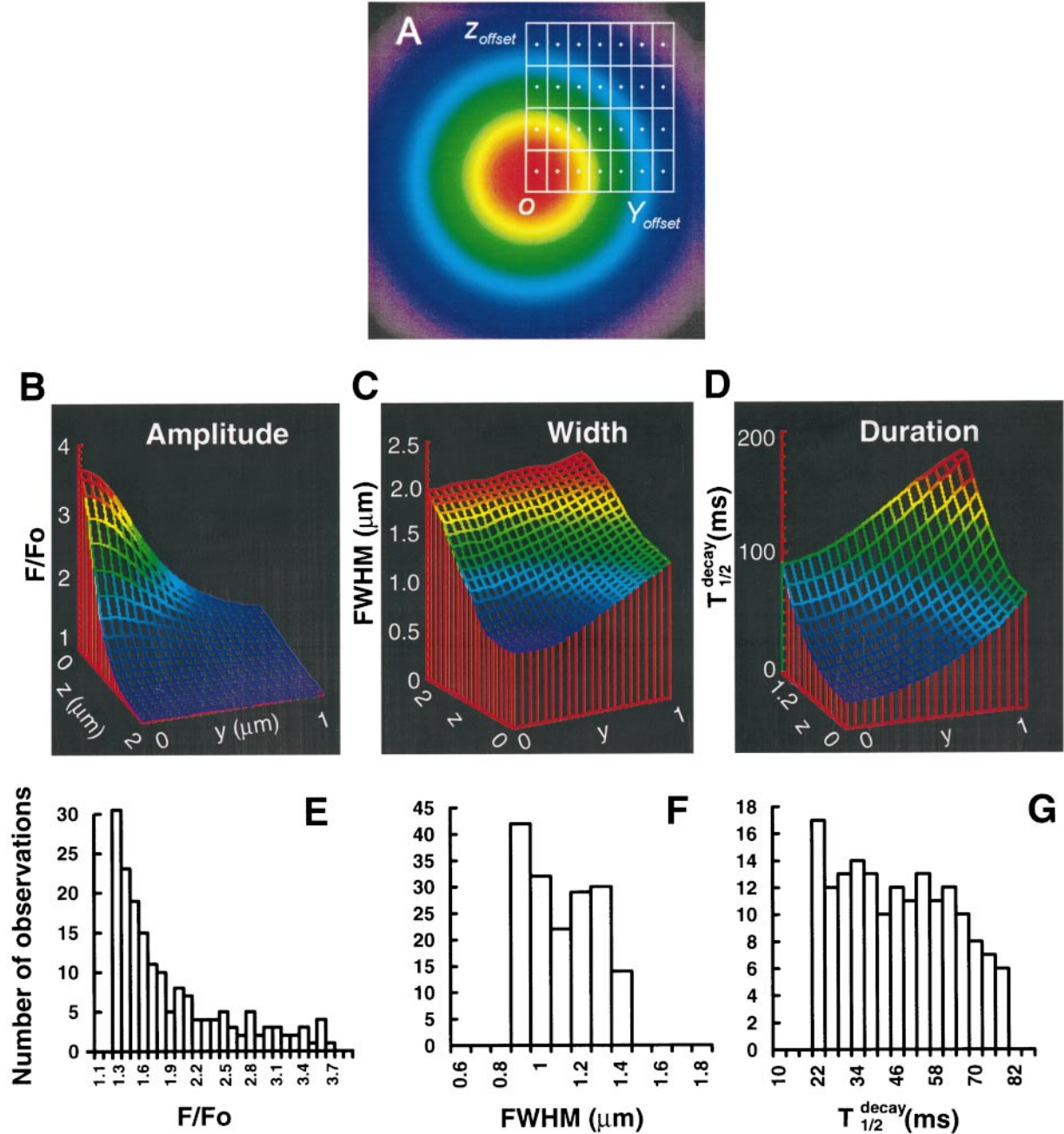


FIGURE 5 Effects of random off-center sampling on experimental parametric measurement of stereotypical  $\text{Ca}^{2+}$  sparks. (A) Position of scan lines in relation to  $\text{Ca}^{2+}$  sparks. Side view of scan lines (crosses) running across  $\text{Ca}^{2+}$  sparks (shaded areas) originated at point O. Direction of linescan is perpendicular to the section plane. A scan line can run right through the spark origin, or more likely, be displaced either laterally ( $Y_{\text{offset}}$ ), or vertically ( $Z_{\text{offset}}$ ), or in both directions. If the scanning line is positioned randomly with respect to the origin of the  $\text{Ca}^{2+}$  spark and the spark is spherically symmetric, we expect the distribution of linescan locations to be uniformly distributed across the section plane. (B–D) Surface plots of spark amplitude (B), width at peak  $F/F_0$  (C) and half-decay time,  $T_{1/2}^{\text{decay}}$  (D) as a function of scan line position ( $y, z$ ). (E–G) Histogram distributions of spark parameters after random sampling. As shown in panel A, the scan line was placed at regular, discrete locations, with  $Y_{\text{offset}}$  and  $Z_{\text{offset}}$  varying from 0–1  $\mu\text{m}$  and 0–2  $\mu\text{m}$  at increments of 0.05  $\mu\text{m}$  and 0.1  $\mu\text{m}$ , respectively. A spark was calculated at each location and the statistics shown are for sparks after thresholding at  $F/F_0 = 1.25$ . Plots are for  $F/F_0$  (E), FWHM (F), and  $T_{1/2}^{\text{decay}}$  (G).



via confocal linescan imaging. All spark parameters exhibit broad distributions with  $F/F_0$  of  $1.9 \pm 0.6$  (mean  $\pm$  SD), FWHM of  $1.1 \pm 0.2 \mu\text{m}$ , and  $T_{1/2}^{\text{decay}}$  of  $48.2 \pm 16.7$  ms. The time to peak fluorescence also increased with distance (data not shown) and had a mean value of  $14.6 \pm 3.1$  ms, which overestimates the  $\text{Ca}^{2+}$  release duration by 46% (10 ms). These calculations are in general agreement with those of Pratusевич and Balke (1996).

Given the transfer functions for spark measurement via confocal imaging (e.g., Fig. 5, *E–G*), what apparent spark statistics should be expected? In our model, the transfer function for spark amplitude follows a monotonic distribution. If multiple populations of  $\text{Ca}^{2+}$  sparks coexist, our model still predicts a monotonic decreasing function for observed spark amplitudes, as long as the apparent amplitude distribution of each subpopulation is a monotonic decreasing function.

In principle, it is possible to back-calculate the intrinsic spark statistics via a deconvolution algorithm using model-derived transfer functions. In practice, the large variance due to detection (Fig. 5; Pratusевич and Balke, 1996) as well as to photon noise (Pratusевич and Balke, 1996) severely comprises our ability to do so. In the simplest case, if all variance in spark statistics were explainable by off-center sampling of a stereotypical event, our model predicts strong intercorrelation among three spark parameters: a strong positive correlation between duration and width ( $\gamma_1$ ,

0.99) and a strong negative correlation between peak and duration ( $\gamma_2$ ,  $-0.88$ ), or width ( $\gamma_3$ ,  $-0.88$ ). To the contrary, experimental data reveal only weak correlation that is sometimes in the opposite direction ( $\gamma_1 = 0.16$ ,  $\gamma_2 = -0.18$ ,  $\gamma_3 = 0.37$ ) (Song et al., 1997). This important negative result indicates that not all sparks are stereotypical and that there must be intrinsic variation among individual release events. Intrinsic variance might be expected on the grounds of stochastic gating of RyR, even if a spark is a collective phenomenon of a cluster of RyR's (Stern, 1992a,b).

### Effects of intrasarcomeric inhomogeneities, anisotropic diffusion, and the geometry of the $\text{Ca}^{2+}$ release site

To investigate the role of spatial inhomogeneities in the shaping of  $\text{Ca}^{2+}$  sparks, we carried out further experiments and simulations using the cylindrical version of our model of  $\text{Ca}^{2+}$  spark formation and detection. Fig. 6 *A* shows a representative confocal image of a rat ventricular myocyte stained with immunofluorescence against the cardiac  $\text{Ca}^{2+}$ -ATPase, SERCA2. In its enlarged view (Fig. 6 *B*), the signal is concentrated along the Z-lines of sarcomeres. Fig. 6 *C* plots the average sarcomeric distribution pattern (*curve a*), which is fit well by a Gaussian function (*curve b*). After deconvolution using our standard PSF parameters to remove

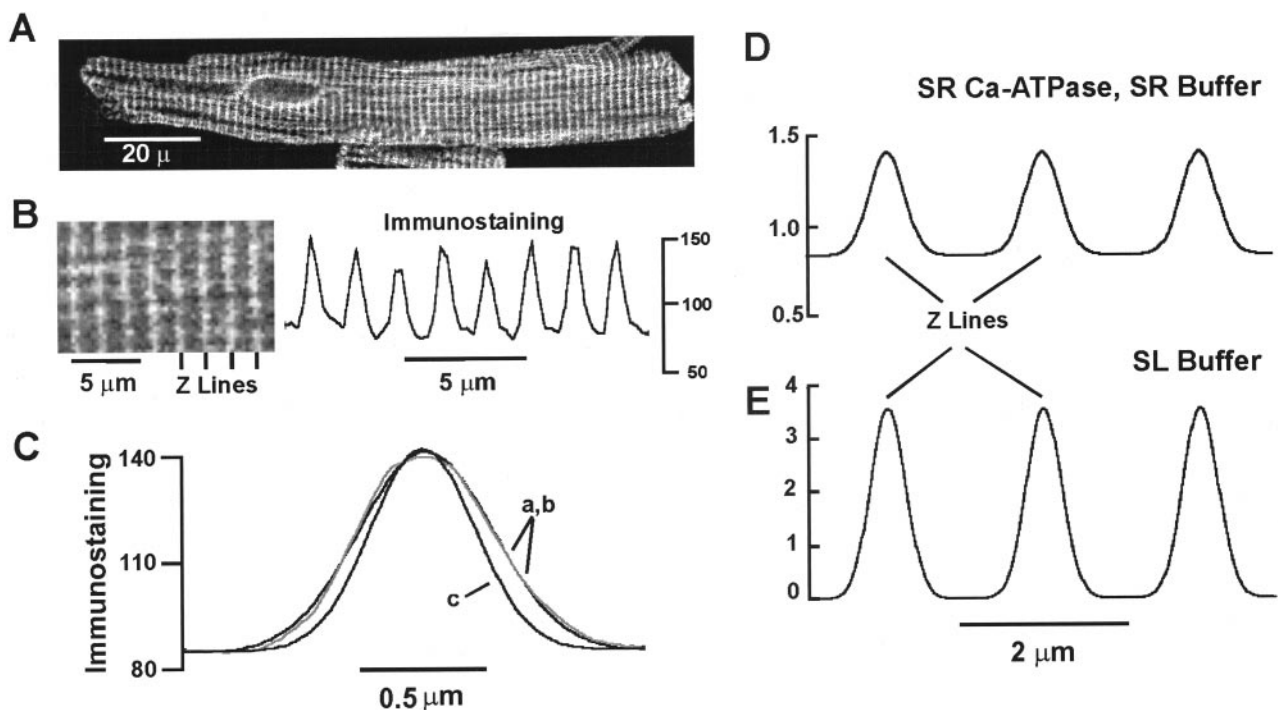


FIGURE 6 Inhomogeneities of  $\text{Ca}^{2+}$  handling mechanisms. (A) A representative immunostaining of rat ventricular myocytes with anti-SERCA2 primary antibody. (B) Enlarged view of eight sarcomeres in *panel A* (left) and the corresponding plot of immunofluorescence distribution (right). Positions of Z-lines are as indicated. Sarcomere length is  $1.8 \mu\text{m}$ . (C) Average immunofluorescence distribution over a sarcomere (*gray line, a*), its Gaussian fit (*dark line, b*), and the fitted profile after deblurring using the PSF in Eq. 9 (*c*). (D–E) Hypothetical function for subsarcomeric distribution of SR  $\text{Ca}^{2+}$  pump and SR buffer (D) and SL buffer (E). These curves are scaled from *curve c* in *panel C*, with (D) and without (E) the basal constant component. In all cases, the value averaged over an entire sarcomere is unity.



optical blurring, the result (*curve c*) consists of two components: a uniform background component reflecting the contribution of the longitudinal SR, and a local bell-shaped component centered around the Z-line that probably reflects the average distribution of the pump at terminal SR. For purposes of the simulation, curve *c* is used to represent the intrasarcomeric distribution of the  $\text{Ca}^{2+}$  pump as well as SR membrane  $\text{Ca}^{2+}$  buffer (Fig. 6 D). We further hypothesize that average sarcolemmal (*t*-tubule) membrane buffer follows the pattern of the local component of the SR but with the background component set to zero (Fig. 6 E).

Representative results of the cylindrical simulations incorporating these longitudinal inhomogeneities are shown in Fig. 7. Because  $\text{Ca}^{2+}$  release occurs at the Z-line (Shacklock et al., 1995; Cheng et al., 1996a), one consequence of the nonuniform distribution of membrane  $\text{Ca}^{2+}$  buffers and SR  $\text{Ca}^{2+}$  pumps is to restrict the  $\text{Ca}^{2+}$  profile 10–20% in the transverse (Z-plane) as compared to the longitudinal direction. In contrast, there was virtually no directional difference for the fluorescence profile, underscoring the fact that fluorescence signals do not always respond to changes in the free  $\text{Ca}^{2+}$  profile. Retrospectively, this result is expected since any directional difference in free  $\text{Ca}^{2+}$  will be attenuated by the diffusion of [CaF]. The observation that sparks are ~20% larger in the long axis than in the short axis of the cell (Cheng et al., 1996b; Parker et al., 1996) must be due to other reasons (e.g., anisotropy in diffusion of  $\text{Ca}^{2+}$  and/or the dye). Fig. 7 also compares these inhomogeneous simulations with the corresponding homogeneous calculation (i.e., a simulation using identical but spatially averaged values for all parameters). In both the transverse and longitudinal directions, the inhomogeneous simulation predicts a more restricted spreading of the  $\text{Ca}^{2+}$  and fluorescence signals and a moderate reduction in signal amplitude. Presumably this is due to the presence of  $\text{Ca}^{2+}$  re-

moval mechanisms (e.g., membrane buffers, pumps) that are preferentially localized near the Z-line in the inhomogeneous simulation. Apart from this small directional difference in  $\text{Ca}^{2+}$ , no further qualitative difference was observed between the homogenous and inhomogeneous versions of the model.

Results on anisotropic diffusion are shown in Fig. 8. Reduction of the transverse diffusion coefficient of either  $\text{Ca}^{2+}$  ( $D_C$ , panel B) or dye ( $D_F$ , panel C) or both (panel D) by 50% leads to a shrinkage in the transverse direction and an expansion of spark in the longitudinal direction, as compared to the isotropic example shown in panel A. (The longitudinal expansion occurs without an increase in the longitudinal diffusion coefficient and reflects diffusion of  $\text{Ca}^{2+}$  preferentially channeled in the direction of least resistance.) Both shrinkage and expansion effectively reproduce the oblong shape of  $\text{Ca}^{2+}$  spark appearance: the eccentricity of sparks (see legend) in panels B, C, and D are 1.18, 1.18, and 1.36, respectively. A directional difference in the  $\text{Ca}^{2+}$  profile was also observed under these conditions (data not shown). Taken together, these calculations and those of the previous paragraph suggest that the asymmetric shape of  $\text{Ca}^{2+}$  sparks is more likely due to anisotropic diffusion of both indicator dye and free  $\text{Ca}^{2+}$  ions (or possibly indicator dye alone), rather than subsarcomeric inhomogeneities of the  $\text{Ca}^{2+}$  buffer and transport system. The microscopic asymmetry of elementary  $\text{Ca}^{2+}$  signaling, albeit small, may be the cause of experimentally observed anisotropies in macroscopic  $[\text{Ca}^{2+}]_i$  dynamics. For example,  $\text{Ca}^{2+}$  waves in heart cells propagate 30% to 55% faster longitudinally than transversely (Engel et al., 1994) even though release sites are separated, on average, about three times farther apart in this direction (Carl et al., 1995; Parker et al., 1996).

FIGURE 7 Simulations comparing  $[\text{Ca}^{2+}]$  (solid lines) and [CaF] (dotted lines) profiles at  $t = 10$  ms for homogeneous and inhomogeneous versions of the model. Traces labeled *homogeneous* are identical to the  $[F]_T = 50 \mu\text{M}$  traces shown in Fig. 3 D. Traces labeled *longitudinal* and *transverse* are the results of the inhomogeneous (cylindrical) simulation. See text for the model. Note that the  $[\text{Ca}^{2+}]$  profile of the inhomogeneous model is restricted in both longitudinal and transverse directions, but more so in the *transverse* direction, in which total endogenous buffer concentration is highest. On the other hand, this directional difference is not clearly seen in the [CaF] traces, as the mobility of the indicator dye results in a smoothing of the CaF signal.

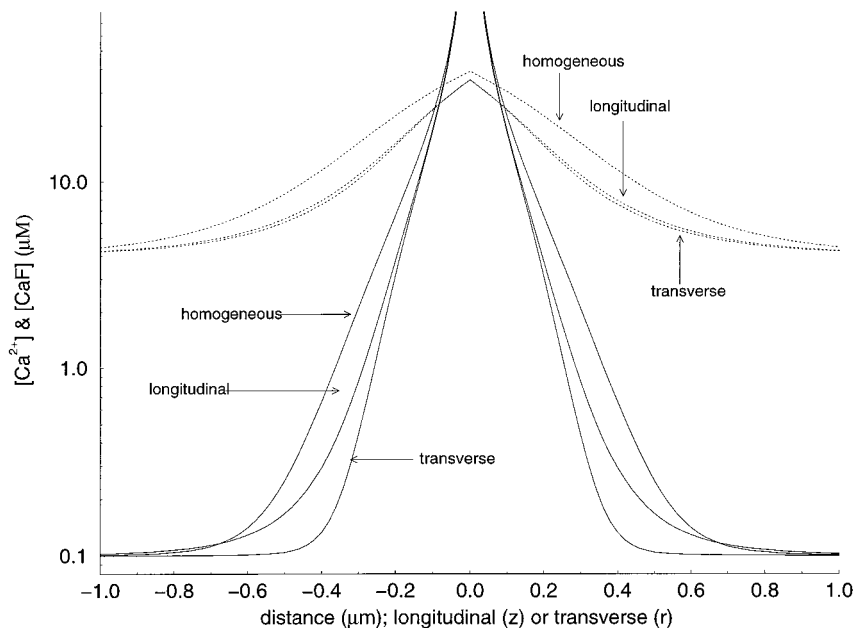
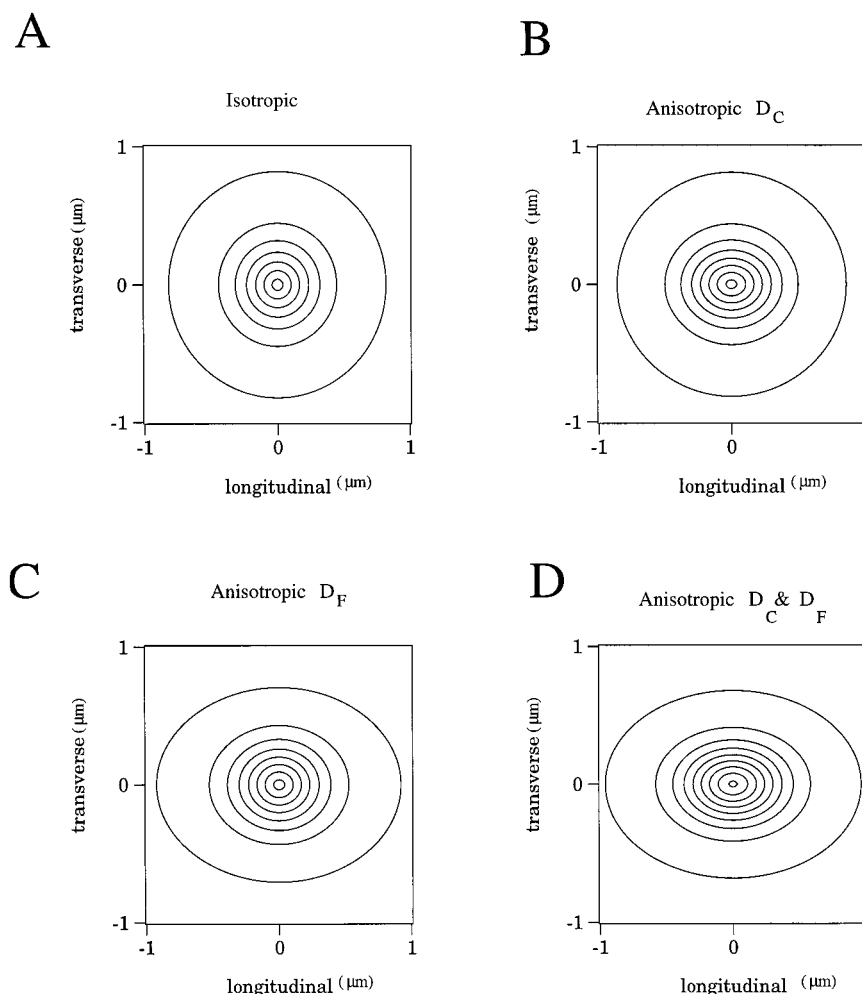


**FIGURE 8** Role of anisotropic diffusion on the appearance of  $\text{Ca}^{2+}$  sparks. Simulated  $\text{Ca}^{2+}$  sparks using standard (A) or 50% reduced values for the diffusion coefficient of  $\text{Ca}^{2+}$  (B) or indicator dye (C) or both (D) in the transverse direction, while keeping the standard values of  $D_C$  and  $D_F$  in the longitudinal direction. Isoconcentration curves (solid lines) are shown for  $[\text{CaF}] = 5$  (outermost), 10, 15, 20, 25, 30, 35, 40, and 45  $\mu\text{M}$ . Calculation does not include spatial averaging due to PSF. A measure of the longitudinal extent of the spark ( $L_Z$ ), defined as the longitudinal extent of the  $[\text{CaF}] = 10 \mu\text{M}$  isoconcentration curve (second outermost), as well as the transverse extent ( $L_R$ , here the smaller value), and eccentricity ( $E = L_Z/L_R$ ) are presented for each calculation. (A) *Isotropic*: neither  $D_C$  nor  $D_F$  reduced; peak  $[\text{CaF}] = 38.7 \mu\text{M}$  and both  $L_Z$  and  $L_R$  are  $0.96 \mu\text{m}$ , giving eccentricity ( $E$ ) of 1.0. (B) *Anisotropic  $D_C$* :  $D_C$ , but not  $D_F$ , is reduced in transverse direction. Peak  $[\text{CaF}] = 43.1 \mu\text{M}$ ,  $L_Z = 1.08 \mu\text{m}$ ,  $L_R = 0.92 \mu\text{m}$ ,  $E = 1.17$ . (C) *Anisotropic  $D_F$* :  $D_F$  but not  $D_C$  is reduced in transverse direction. Peak  $[\text{CaF}] = 43.3 \mu\text{M}$ ,  $L_Z = 1.02 \mu\text{m}$ ,  $L_R = 0.92 \mu\text{m}$ ,  $E = 1.21$ . (D) *Anisotropic  $D_C$  and  $D_F$* : both  $D_C$  and  $D_F$  are reduced in transverse direction. Peak  $[\text{CaF}] = 46.7 \mu\text{M}$ ,  $L_Z = 1.24 \mu\text{m}$ ,  $L_R = 0.88 \mu\text{m}$ ,  $E = 1.41$ . Note that the *anisotropic  $D_F$*  case is slightly more eccentric than the *anisotropic  $D_C$*  case, and that a 50% reduction in either diffusion coefficient alone results in the experimentally observed eccentricity of 20% (Cheng et al., 1996).



We also used the cylindrical version of our model of  $\text{Ca}^{2+}$  spark formation and detection to investigate the role of the geometry of the  $\text{Ca}^{2+}$  release site on the shape of  $\text{Ca}^{2+}$  sparks. For example, Fig. 9 A shows isoconcentration curves (solid lines) for the  $\text{CaF}$  profile of a simulated  $\text{Ca}^{2+}$  spark using standard parameters, except that  $\text{Ca}^{2+}$  release is spatially distributed over a ring  $0.6 \mu\text{m}$  in diameter, representing the entry of  $\text{Ca}^{2+}$  into the cytosol via the opening of a diad cleft. When spatial averaging due to the PSF is not included (Fig. 9 A), the  $\text{CaF}$  profile responds to the geometry of the  $\text{Ca}^{2+}$  release and the spatially extended source creates a spark that is elongated in the plane of the ring. However, when spatial averaging is included (e.g., using a spherical PSF with  $\text{FWHM} = 0.4 \mu\text{m}$  in Fig. 9 B and  $0.6 \mu\text{m}$  in Fig. 9 C), the ring geometry of the source is obscured and the eccentricity of the  $\text{Ca}^{2+}$  spark is reduced. In addition, the ring geometry of the source in these cylindrical simulations produces only a modest increase in the  $\text{FWHM}$  of the spark in the plane of the ring ( $\text{FWHM}_R = 1.04 \mu\text{m}$  in Fig. 9 B and  $1.08 \mu\text{m}$  in Fig. 9 C). Considering the source diameter was increased by  $0.6 \mu\text{m}$ , these values represent only a small increase in the  $\text{FWHM}$  over that of the standard spherical spark of Fig. 1 D ( $\text{FWHM} = 0.89 \mu\text{m}$ ). Once

again, we observe that the  $\text{FWHM}$  is a  $\text{Ca}^{2+}$  spark measure that is relatively insensitive to model parameters.

## DISCUSSION

Although the problem of  $\text{Ca}^{2+}$  diffusion from open channel mouth into buffer-containing medium has been studied by many investigators (e.g., Stern, 1992a,b; Langer and Peskoff, 1996; Soeller and Cannell, 1997), the present work shows that in the context of fluorescent measurement, the  $\text{Ca}^{2+}$  signal may not be directly translated into the signal reported by the indicator, and that the  $\text{Ca}^{2+}$  signal per se may be altered by the presence of the indicator. The present model of  $\text{Ca}^{2+}$  spark formation explicitly solves equations for the diffusion of both free  $\text{Ca}^{2+}$  and indicator (Cheng et al., 1993, 1995; Gómez et al., 1996). There are two major differences in the model reported here when compared to the model of Pratusевич and Balke (1996): 1) the present work emphasizes  $\text{Ca}^{2+}$  spark formation mechanisms and also the relation between the increase in fluorescence and the elevation of the underlying  $[\text{Ca}^{2+}]_i$ , issues complementary to those involved in spark detection, such as optical

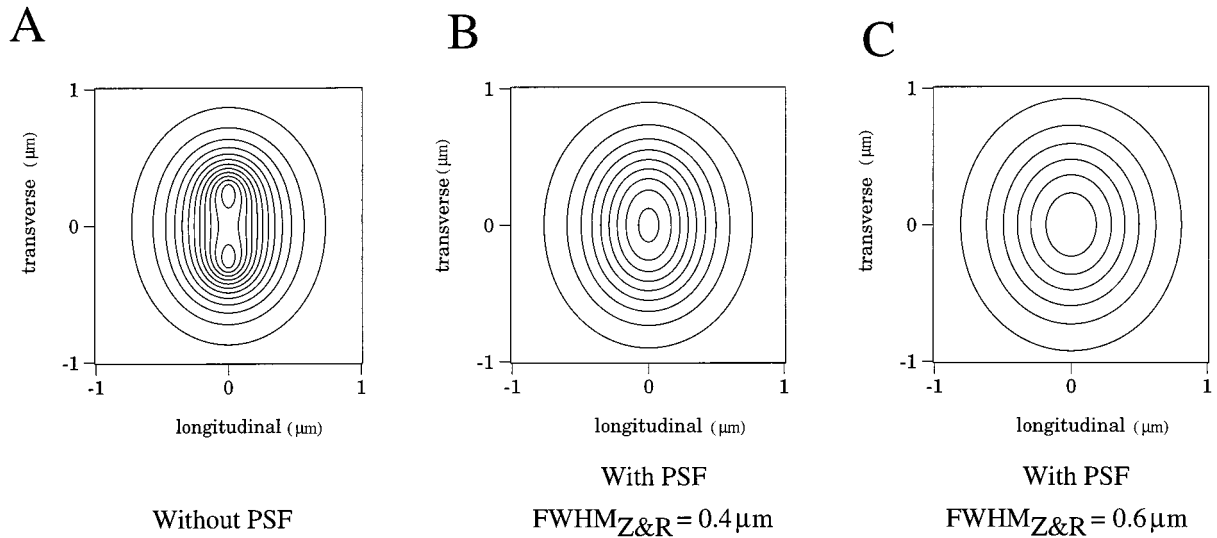


FIGURE 9 Simulated  $\text{Ca}^{2+}$  spark using standard parameters except that  $\text{Ca}^{2+}$  release is spatially distributed over a ring  $0.6 \mu\text{m}$  in diameter, representing the entry of  $\text{Ca}^{2+}$  into the cytosol via the opening of a diad cleft. Isoconcentration curves (solid lines) are shown for  $[\text{CaF}]$  of  $5 \mu\text{M}$  and successively higher concentrations at  $1 \mu\text{M}$  intervals. A measure of the longitudinal extent of the spark ( $L_z$ ), defined as the longitudinal extent of the  $[\text{CaF}] = 10 \mu\text{M}$  isoconcentration curve, as well as the transverse extent ( $L_R$ , here the larger value), and eccentricity ( $E = L_z/L_R$ ) are presented for each calculation. Time is  $10 \text{ ms}$ . (A) This calculation does not include spatial averaging due to PSF. Note that one consequence of distributing the  $\text{Ca}^{2+}$  release over a ring  $0.6 \mu\text{m}$  in diameter is to create a spark which is elongated in the plane of the ring ( $L_z = 0.60 \mu\text{m}$ ,  $L_R = 0.96 \mu\text{m}$ , and  $E = L_z/L_R = 0.63$ ). The innermost isoconcentration curves indicate  $[\text{CaF}] = 16 \mu\text{M}$ . (B) Calculation shown in (A) after spatial averaging with a spherical PSF ( $\text{FWHM}_{xy} = 0.4 \mu\text{m}$  and  $\text{FWHM}_z = 0.4 \mu\text{m}$ ) giving  $L_z = 0.56 \mu\text{m}$ ,  $L_R = 0.80 \mu\text{m}$ , and  $E = 0.70$ . Innermost isoconcentration curve indicates  $[\text{CaF}] = 13 \mu\text{M}$  and the FWHM of the simulated  $\text{Ca}^{2+}$  spark in the longitudinal and transverse directions is  $1.04$  and  $0.76 \mu\text{m}$ , respectively. (C) Calculation shown in (A) after spatial averaging with a larger spherical PSF ( $\text{FWHM}_{xy} = 0.6 \mu\text{m}$  and  $\text{FWHM}_z = 0.6 \mu\text{m}$ ) giving  $L_z = 0.36 \mu\text{m}$ ,  $L_R = 0.44 \mu\text{m}$ , and  $E = 0.82$ . Innermost isoconcentration curve indicates  $[\text{CaF}] = 10 \mu\text{M}$  and the FWHMs of the simulated  $\text{Ca}^{2+}$  spark in the longitudinal and transverse directions are  $1.08$  and  $0.92 \mu\text{m}$ , respectively, slightly greater than (B). Note that in both (B) and (C), out-of-focus fluorescence interferes with resolving the geometry of the source and that low resolution (larger PSF) reduces the observed eccentricity, i.e.,  $E$  is closest to unity in (C). Also note that the ring geometry of the source in this cylindrical simulation increases the FWHM of the spark only slightly over the standard spherical spark of Fig. 1 D, where  $\text{FWHM} = 0.89 \mu\text{m}$ .

blurring, photon noise, and detectability; 2) the mobility of the indicator dye is included as factor in the model presented here. As shown in Fig. 3, neglect of dye diffusion altogether introduces large errors in the amplitude, time to peak, relaxation, and spatial spreading of the simulated spark. In the previous model, an extremely high SR  $\text{Ca}^{2+}$ -ATPase activity (spatially averaged  $V_{\text{max}} \sim 44,444 \mu\text{M/s}$  vs.  $208 \mu\text{M/s}$  reported in Bassani et al., 1994) and a high free  $\text{Ca}^{2+}$  diffusion coefficient ( $600 \mu\text{m}^2/\text{s}$ ) compensates for the effect of dye immobilization. Furthermore, their model assumes a latticelike distribution of RyR's, a discrete distribution of the SR pump on longitudinal and transverse planes separated  $0.675 \mu\text{m}$  apart, and a discontinuity of  $\text{Ca}^{2+}$  diffusion coefficient across these planes. The scenarios of spark formation mechanisms presented in the two models are thus very different. Computationally, their choice of geometry requires a 3-D simulation (with eightfold symmetry), whereas the simplicity of the present model allows us to comprehensively explore different parameter settings. In both the present model and the model by Pratusevich and Balke, details on structure,  $\text{Ca}^{2+}$  binding, and surface charges inside the diad cleft, where junctional RyR's reside, have not been included. The importance of these nanoscale features in the establishment and dissipation of  $\text{Ca}^{2+}$  gradient *within* the diadic space has recently been modeled in

the context of cardiac excitation-contraction coupling (Soeller and Cannell, 1997) and  $\text{Ca}^{2+}$  extrusion via the SL  $\text{Na}^+/\text{Ca}^{2+}$  exchange (Langer and Peskoff, 1996).

The model of Pratusevich and Balke (1996) predicts a monotonic spark amplitude distribution when the observation line is positioned randomly with respect to the origin of the spark (see also Fig. 5 E), but a multimodal distribution when repeated observations of randomly occurring sparks are made from the same scan line. The latter seems to stem from their assumption that release sites form a rigorous lattice in Z-planes and that the pattern is strictly in register over all Z-planes (which is unlikely inside the cell). While observations in which sparks were selected by eye have often indicated an amplitude distribution consisting of one or more Gaussian components (Klein et al., 1996; Lukyanenko et al., 1996; Satoh et al., 1997; Xiao et al., 1997), more recent studies suggest another explanation for the experimentally observed modal distribution. With automated computer algorithms to count and measure  $\text{Ca}^{2+}$  sparks, about twice as many  $\text{Ca}^{2+}$  sparks (often in the low amplitude end) can now be detected and the amplitude distributions in both cardiomyocytes (Song et al., 1997) and skeletal muscle cells (E. Rios, personal communication) are consistent with a monotonic decreasing function, subjected to detection thresholding. This is consistent with the results

presented here and suggests that reported modal distributions could be due to the observer's selection bias against small amplitude events (rather than to ultrastructural regularity). Additionally, spark statistics may have multiple modes when the assumption of randomness is violated, e.g., statistics dominated by events from some particular sites exhibiting repetitive activities (Cheng et al., 1993; Tsugorka et al., 1995; Parker et al., 1996).

In the present study, we have demonstrated that a simple numerical model provides a very useful investigative tool for understanding the mechanism of  $\text{Ca}^{2+}$  spark formation and detection. Many salient features of  $\text{Ca}^{2+}$  sparks, including the amplitude, the kinetics, the oblong shape, as well as the modulation by physiological factors, are reproduced using the radial and cylindrical versions of the model. However, we have been unable to quantitatively reproduce the spatial size of the  $\text{Ca}^{2+}$  spark, indicating that our understanding of spark formation, as reflected in the model's structure and parameters, is still limited. More importantly, our calculations reveal three generic problems confronting the interpretation of fluorescence signal: 1) the fluorescence signal differs markedly from the underlying  $\text{Ca}^{2+}$  signal; 2) interpretation of fluorescence data (e.g., peak intensity) can be equivocal; and 3) differences seen in the fluorescence signal do not always match changes in  $\text{Ca}^{2+}$  signal, and it is equally true that not all changes in  $\text{Ca}^{2+}$  signal are accompanied by a similar change in fluorescence signal. Furthermore, the model cautions us that near millimolar concentrations of fluo-3-like indicator could disturb the  $\text{Ca}^{2+}$  signaling process of interest. Since indicator fluorescence has a complicated relationship to the underlying  $\text{Ca}^{2+}$  fluxes, and since  $\text{Ca}^{2+}$  spark statistics are contaminated with large variance due to limitations of contemporary confocal microscopy, computer modeling plays an important role in data interpretation and experiment design. Meanwhile, a new generation of  $\text{Ca}^{2+}$  indicators and optical techniques is required to resolve microscopic and nanoscopic  $\text{Ca}^{2+}$  signaling on the millisecond scale.

## APPENDIX: NUMERICAL METHODS

The Laplacian operator simplifies in the case of cylindrical symmetry to

$$\nabla^2 = \frac{1}{r} \frac{\partial}{\partial r} \left( r \frac{\partial}{\partial r} \right) \hat{r} + \frac{\partial^2}{\partial z^2} \quad (a1)$$

$$\hat{z} = \left( \frac{\partial^2}{\partial r^2} + \frac{1}{r} \frac{\partial}{\partial r} \right) \hat{r} + \frac{\partial^2}{\partial z^2} \hat{z} \quad (r > 0)$$

We can deal with the singularity of the polar form of the Laplacian at  $r = 0$  by replacing Eq. a1 with its Cartesian equivalent,  $\nabla^2 = (\partial^2/\partial x^2)\hat{x} + (\partial^2/\partial y^2)\hat{y} + (\partial^2/\partial z^2)\hat{z}$ . Cylindrical symmetry implies that the first two components of the Cartesian Laplacian have equal magnitudes. This allows us to approximate the polar Laplacian at the origin by

$$\nabla^2 \approx 2 \frac{\partial^2}{\partial r^2} \hat{r} + \frac{\partial^2}{\partial z^2} \hat{z} \quad (r = 0)$$

(see pp. 75–76 of Smith, 1985). Thus we can write

$$L(U_{0,j}^n) = \frac{2}{\Delta r^2} [2U_{1,j}^n - 2U_{0,j}^n] + \frac{1}{\Delta z^2} [U_{0,j+1}^n - 2U_{0,j}^n + U_{0,j-1}^n] \quad (a2)$$

for  $i = 0$ ,

$$L(U_{i,0}^n) = \frac{1}{r_i \Delta r^2} [r_{i+1/2}(U_{i+1,j}^n - U_{i,j}^n) - r_{i-1/2}(U_{i,j}^n - U_{i-1,j}^n)] + \frac{1}{\Delta z^2} [2U_{i,1}^n - 2U_{i,0}^n] \quad (a3)$$

for  $j = 0$ , and

$$L(U_{i,j}^n) = \frac{1}{r_i \Delta r^2} [r_{i+1/2}(U_{i+1,j}^n - U_{i,j}^n) - r_{i-1/2}(U_{i,j}^n - U_{i-1,j}^n)] + \frac{1}{\Delta z^2} [U_{i,j+1}^n - 2U_{i,j}^n + U_{i,j-1}^n] \quad (a4)$$

for  $i > 0$  and  $j > 0$ , where  $U_{i,j}^n$  is an approximation to the function  $u(r_i, z_j, t_n)$ ,  $u$  represents any of the species in Eqs. 2–4,  $r_i = i\Delta r$ ,  $z_j = j\Delta z$ ,  $t_n = n\Delta t$ ,  $L(U_{i,j}^n)$  is the approximation to the Laplacian at the point  $(r_i, z_j, t_n)$ , and we have used a “reflective” boundary condition  $(\partial u/\partial r)|_{r=0} = 0$ , in its discretized form,  $U_{-1}^n = U_1^n$ . For all species save  $\text{Ca}^{2+}$ , this boundary condition can be interpreted as a “no flux” condition at the origin, meaning that no mobile species can be transported via diffusion either into or out of the domain of the simulation. In the case of  $\text{Ca}^{2+}$ , the free species is introduced at the origin in accordance with the time-dependence of  $\sigma_{\text{ryr}}$  so that  $\lim_{t \rightarrow 0} \{-2\pi r^2 D_c (\partial[\text{Ca}^{2+}]/\partial r)\} = \sigma_{\text{ryr}}$  is always satisfied, that is, at each time step we increase the concentration of  $\text{Ca}^{2+}$  at the origin ( $[\text{Ca}^{2+}]_0$ ), at a rate in accordance with the reaction term  $J_{\text{ryr}} = \sigma_{\text{ryr}} \delta(\vec{r})$ . The rate of change in  $\text{Ca}^{2+}$  concentration at the origin due to the presence of the source ( $\sigma_{\text{ryr}}$ ) depends on the source strength and the volume which the mesh point at the origin “represents,” that is, a cylinder with radius  $\Delta r/2$  and height  $\Delta z/2$ , with volume  $V = \pi(\Delta r/2)^2(\Delta z/2)$ . Using Faraday's law,  $\sigma_{\text{ryr}} = i_{\text{Ca}}/2F$ , where  $i_{\text{Ca}}$  is the current amplitude of the source, and  $F$  is Faraday's constant ( $F = 9.648 \times 10^4$  coul/mol), the rate of change in  $[\text{Ca}^{2+}]$  at the origin due to the presence of the release site is

$$J_{\text{ryr}} = \frac{\sigma_{\text{ryr}}}{V} = \frac{8i_{\text{Ca}}^*(5.128 \times 10^3 \mu\text{M s}^{-1})}{\pi(\Delta r^*)^2 \Delta z^*} \quad (a5)$$

where  $i_{\text{Ca}}^*$  is the source strength measured in picoamps, and  $\Delta r^*$  and  $\Delta z^*$  are the mesh size measured in micrometers.

Using the above equations, an explicit numerical scheme that is second-order accurate in space and first-order accurate in time is given by

$$\frac{U_{i,j}^{n+1} - U_{i,j}^n}{\Delta t} = D_u L(U_{i,j}^n) + RXN(U_{i,j}^n) \quad (a6)$$

where  $D_u$  is the diffusion constant for species  $u$  and  $RXN(U_{i,j}^n)$  denotes the contribution of the appropriate reaction terms in Eqs. 2–4. Of course,  $L(U_{i,j}^n)$  evaluates to zero when  $u$  denotes a stationary  $\text{Ca}^{2+}$  buffer, since in that case  $D_u = 0$ .

These calculations were performed on a Silicon Graphics Indigo 2 workstation. In addition to the explicit numerical scheme presented here, we coded a second version using an alternate direction implicit numerical scheme that produced identical results.

The authors thank Mark B. Cannell for initial discussion on spark modeling, C. F. Neubauer for experiments with immunofluorescence, and Arthur Sherman and Edward G. Lakatta for reading this manuscript.



This work is supported by National Institutes of Health intramural research programs (to H.C. and M.D.S.), a National Institutes of Health IRTA fellowship (to G.S.), National Institutes of Health grants (to J.K. and W.J.L.), and the Agricultural Experiment Station at University of California Davis (J.K.).

## REFERENCES

- Allbritton, N. L., T. Meyer, and L. Stryer. 1992. Range of messenger action of  $\text{Ca}^{2+}$  ion and inositol 1,4,5-trisphosphate. *Science*. 258:1812–1815.
- Balke, C. W., T. M. Egan, and W. G. Wier. 1994. Processes that remove calcium from the cytoplasm during excitation-contraction coupling in intact rat heart cells. *J. Physiol. (Lond.)*. 474:447–472.
- Bassani, J. W. M., R. A. Bassani, and D. M. Bers. 1994. Relaxation in rabbit and rat cardiac cells: species-dependent differences in cellular mechanisms. *J. Physiol. (Lond.)*. 476:279–293.
- Berridge, M. 1993. Inositol trisphosphate and calcium signaling. *Nature*. 361:315–325.
- Bers, D. M. 1991. Excitation-Contraction Coupling and Cardiac Contractile Force. Kluwer Academic Publishers, The Netherlands.
- Bers, D. M., K. D. Philipson, and A. Peskoff. 1985. Calcium at the surface of cardiac plasma membrane vesicles: cation binding, surface charge screening, and Na-Ca exchange. *J. Membr. Biol.* 85:251–261.
- Blatter, L. A., J. Hüser, and E. Riós. 1997. Sarcoplasmic reticulum  $\text{Ca}^{2+}$  release flux underlying  $\text{Ca}^{2+}$  sparks in cardiac muscle. *Proc. Natl. Acad. Sci. USA*. 94:4176–4181.
- Cannell, M. B., H. Cheng, and W. J. Lederer. 1995. The control of calcium release in heart muscle. *Science*. 268:1045–1049.
- Carl, S. L., K. Felix, A. H. Caswell, N. R. Brandt, W. J. Ball, Jr., P. L. Vaghy, G. Meissner, and D. G. Ferguson. 1995. Immunolocalization of sarcolemmal dihydropyridine receptor and sarcoplasmic reticular triadin and ryanodine receptor in rabbit ventricle and atrium. *J. Cell Biol.* 129:673–682.
- Cheng, H., M. B. Cannell, and W. J. Lederer. 1995. Partial inhibition of  $\text{Ca}^{2+}$  current by methoxyverapamil (D600) reveals spatial nonuniformities in  $[\text{Ca}^{2+}]_i$  during excitation-contraction coupling in cardiac myocytes. *Circ. Res.* 76:236–241.
- Cheng, H., W. J. Lederer, and M. B. Cannell. 1993. Calcium sparks: elementary events underlying excitation-contraction coupling in heart muscle. *Science*. 262:740–744.
- Cheng, H., M. R. Lederer, W. J. Lederer, and M. B. Cannell. 1996a. Calcium sparks and  $[\text{Ca}^{2+}]_i$  waves in cardiac myocytes. *Am. J. Physiol.* 270:C148–C159.
- Cheng, H., M. R. Lederer, R.-P. Xiao, A. M. Gómez, Y.-Y. Zhou, B. Ziman, H. Spurgeon, E. G. Lakatta, and W. J. Lederer. 1996b. Excitation-contraction coupling in heart: new insights from  $\text{Ca}^{2+}$  sparks. *Cell Calcium*. 20:129–140.
- Eberhard, M., and P. Erne. 1989. Kinetics of calcium binding to fluo-3 determined by stopped-flow fluorescence. *Biochem. Biophys. Res. Commun.* 163:309–314.
- Engel, J., M. Fechner, A. J. Sowerby, S. A. E. Finch, and A. Stier. 1994. Anisotropic propagation of  $\text{Ca}^{2+}$  waves in isolated cardiomyocytes. *Biophys. J.* 66:1756–1762.
- Fabiato, A. 1985. Time- and calcium-dependence of activation and inactivation of calcium-induced release of calcium from the sarcoplasmic reticulum of a skinned cardiac Purkinje cell. *J. Gen. Physiol.* 85:247–290.
- Gómez, A., H. Cheng, W. J. Lederer, and D. M. Bers. 1996.  $\text{Ca}^{2+}$  diffusion and sarcoplasmic reticulum transport both contribute to  $[\text{Ca}^{2+}]_i$  decline during  $\text{Ca}^{2+}$  sparks in rat ventricular myocytes. *J. Physiol. (Lond.)*. 496:575–581.
- Harkins, A. B., N. Kurebayashi, and S. M. Baylor. 1993. Resting myoplasmic free calcium in frog skeletal muscle fibers estimated with fluo-3. *Biophys. J.* 65:865–881.
- Horne, J. H., and T. Meyer. 1997. Elementary calcium-release units induced by inositol trisphosphate. *Science*. 276:1690–1693.
- Kieval, R. S., R. J. Bloch, G. E. Lindenmayer, A. Ambesi, and W. J. Lederer. 1992. Immunofluorescence localization of the Na-Ca exchanger in heart cells. *Am. J. Physiol.* 263:C545–C550.
- Klein, M. G., H. Cheng, L. F. Santana, Y.-H. Jiang, W. J. Lederer, and M. F. Schneider. 1996. Two mechanisms of quantized calcium release in skeletal muscle. *Nature*. 379:455–458.
- Langer, G. A., and A. Peskoff. 1996. Calcium concentration and movement in the diadic cleft space of the cardiac ventricular cell. *Biophys. J.* 70:1169–1182.
- Lipp, P., and E. Niggli. 1996. Submicroscopic calcium signals as fundamental events of excitation-contraction coupling in guinea-pig cardiac myocytes. *J. Physiol. (Lond.)*. 492:31–38.
- López-López, J. R., P. S. Shacklock, C. W. Balke, and W. G. Wier. 1995. Local calcium transients triggered by single L-type calcium channel currents in cardiac cells. *Science*. 268:1042–1045.
- Lukyanenko, V., I. Györke, and S. Györke. 1996. Regulation of calcium release by calcium inside the sarcoplasmic reticulum in ventricular myocytes. *Pflügers Arch.* 432:1047–1054.
- Morton, K. W., and D. F. Mayers. 1994. Numerical Solution of Partial Differential Equations: An Introduction. Cambridge University Press, Cambridge, UK.
- Neher, E. 1986. Concentration profiles of intracellular  $\text{Ca}^{2+}$  in the presence of diffusible chelator. *Exp. Brain Res.* 14:80–96.
- Nelson, M. T., H. Cheng, M. Rubart, L. F. Santana, A. D. Bonev, H. J. Knot, and W. J. Lederer. 1995. Relaxation of arterial smooth muscle by calcium sparks. *Science*. 270:633–637.
- Parker, I., and Y. Yao. 1996.  $\text{Ca}^{2+}$  transients associated with openings of inositol trisphosphate-gated channels in *Xenopus* oocytes. *J. Physiol. (Lond.)*. 491:663–668.
- Parker, I., W. J. Zang, and W. G. Wier. 1996.  $\text{Ca}^{2+}$  sparks involving multiple  $\text{Ca}^{2+}$  release sites along Z-lines in rat heart cells. *J. Physiol. (Lond.)*. 497:31–38.
- Post, J. A., and G. A. Langer. 1992. Sarcolemmal calcium binding sites in heart. I. Molecular origin in “gas-dissected” sarcolemma. *J. Membr. Biol.* 129:49–57.
- Pratusevich, V. R., and C. W. Balke. 1996. Factors shaping the confocal image of the calcium spark in cardiac muscle cells. *Biophys. J.* 71:2942–2957.
- Roberts, W. M. 1993. Spatial  $\text{Ca}^{2+}$  buffering in saccular hair cells. *Nature*. 363:74–76.
- Satoh, H., L. A. Blatter, and D. M. Bers. 1997. Effects of  $[\text{Ca}^{2+}]_i$ , SR  $\text{Ca}^{2+}$  load, and rest on  $\text{Ca}^{2+}$  spark frequency in ventricular myocytes. *Am. J. Physiol.* 272:H657–H668.
- Shacklock, P. S., W. G. Wier, and C. W. Balke. 1995. Local  $\text{Ca}^{2+}$  transients ( $\text{Ca}^{2+}$ -sparks) originate at transverse tubules in rat heart cells. *J. Physiol. (Lond.)*. 487:601–608.
- Sham, J. S. 1997.  $\text{Ca}^{2+}$  release-induced inactivation of  $\text{Ca}^{2+}$  current in rat ventricular myocytes: evidence for local  $\text{Ca}^{2+}$  signaling. *J. Physiol. (Lond.)*. 500:285–295.
- Sipido, K. R., and W. G. Wier. 1991. Flux of  $\text{Ca}^{2+}$  across the sarcoplasmic reticulum of Guinea-pig cardiac cells during excitation-contraction coupling. *J. Physiol. (Lond.)*. 435:605–630.
- Smith, G. D. 1985. Numerical Solution of Partial Differential Equations: Finite Difference Methods. Oxford Applied Mathematics and Computing Science Series, 3rd ed. Clarendon Press, Oxford, UK. 75–76.
- Smith, G. D. 1996. Analytical steady-state solution to the rapid buffering approximation near an open  $\text{Ca}^{2+}$  channel. *Biophys. J.* 71:3064–3072.
- Smith, G., J. Wagner, and J. Keizer. 1996. Validity of the rapid buffering approximation near a point source of  $\text{Ca}^{2+}$  ions. *Biophys. J.* 70:2527–2539.
- Soeller, C., and M. B. Cannell. 1997. Numerical simulation of local calcium movements during L-type calcium channel gating in the cardiac diad. *Biophys. J.* 73:97–111.
- Song, L.-S., M. D. Stern, E. G. Lakatta, and H. Cheng. 1997. Partial depletion of sarcoplasmic reticulum calcium does not prevent calcium sparks in rat ventricular myocytes. *J. Physiol. (Lond.)*. 505:655–675.
- Stern, M. D. 1992a. Buffering of  $\text{Ca}^{2+}$  in the vicinity of a channel pore. *Cell Calcium*. 13:183–192.
- Stern, M. D. 1992b. Theory of excitation-contraction coupling in cardiac muscle. *Biophys. J.* 63:497–517.

- Sun, X.-H., F. Protasi, M. Takahashi, H. Takeshima, D. G. Ferguson, and C. Franzini-Armstrong. 1995. Molecular architecture of membranes involved in excitation-contraction coupling of cardiac muscle. *J. Cell Biol.* 129:659–671.
- Tinker, A., A. R. G. Lindsay, and A. J. Williams. 1993. Cation conductance in the calcium release channel of the cardiac sarcoplasmic reticulum under physiological and pathophysiological conditions. *Cardiovasc. Res.* 27:1820–1825.
- Tsugorka, A., E. Riós, and L. A. Blatter. 1995. Imaging elementary events of calcium release in skeletal muscle cells. *Nature.* 269:1723–1726.
- Wagner, J., and J. Keizer. 1994. Effects of rapid buffers on  $\text{Ca}^{2+}$  diffusion and  $\text{Ca}^{2+}$  oscillations. *Biophys. J.* 67:447–456.
- Wang, J. H. 1953. Tracer-diffusion in liquid. IV. Self-diffusion of calcium ion and chloride ion in aqueous calcium chloride solutions. *J. Am. Chem. Soc.* 75:1769–1770.
- Wang, W., Y. J. Suzuki, L. Cleemann, L. R. Jones, and M. Morad. 1997.  $\text{Ca}^{2+}$  sparks and  $\text{Ca}^{2+}$  release in transgenic myocytes overexpressing cardiac calsequestrin. *Biophys. J.* 72:44a (Abstr.).
- Xiao, R.-P., H. H. Valdivia, K. Bogdanov, C. Valdivia, E. G. Lakatta, and H. Cheng. 1997. The immunophilin FK506 binding protein (FKBP) modulates  $\text{Ca}^{2+}$  release channel closure in rat heart. *J. Physiol. (Lond.)*. 500:331–342.
- Yao, Y., J. Choi, and I. Parker. 1995. Quantal puffs of intracellular  $\text{Ca}^{2+}$  evoked by  $\text{IP}_3$  in *Xenopus* oocytes. *J. Physiol. (Lond.)*. 491:663–668.